J. Fluid Mech. (2004), *vol.* 514, *pp.* 77–105.
DOI: 10.1017/S002211200400031X Printed in the United Kingdom

A numerical and experimental study on advection in three-dimensional Stokes flows

By M. F. M. SPEETJENS, H. J. H. CLERCX AND G. J. F. VAN HEIJST

Fluid Dynamics Laboratory, Department of Physics, Eindhoven University of Technology, P.O. Box 513, 5600 MB Eindhoven, The Netherlands

(Received 23 June 2003 and in revised form 26 April 2004)

Three-dimensional advection of passive tracers in non-inertial flows is studied in a finite cylinder confined by two parallel endwalls by means of numerical simulations and laboratory experiments. The fluid is set in motion through steady or time-periodic forcing by in-plane motion of the endwalls via a given forcing protocol. The numerical analysis centres on a dynamical-systems approach and concerns symmetry-based identification of coherent structures in the web of tracer paths (collectively defining the flow topology) for a number of archetypal flow configurations. The role of the flow topology in the process of tracer transport is investigated by numerical tracking of finite-size material objects released at strategic locations in the flow. Experimental validation of key aspects of the numerical results has been carried out in laboratory experiments by flow visualization with dye and flow measurement via three-dimensional particle tracking velocimetry.

1. Introduction

In a fluid-dynamical context the concept of 'mixing' refers to physical processes in which two or more liquid substances are combined in such way that each individual fluid is continuously distributed among the other fluids. Instances of mixing arise in manifold forms in a wide variety of situations and disciplines. Mixing is fundamental to many transport phenomena studied in astrophysics, geology, geophysics and physiology. Numerous industrial activities (e.g. food processing, polymer blending, petrochemical processing) involve fluid mixing in one form or another. Even at a domestic level mixing is widespread; consider e.g. everyday proceedings such as whipping of cream, stirring of coffee and dispersion of detergents.

Mixing processes span an enormous range of length and time scales and encompass Reynolds numbers varying over forty orders of magnitude (see Ottino 1990). Moreover, mixing flows typically involve a complex interplay among mass transport and molecular effects, rheological properties, multiphase effects, chemical reaction and heat transfer. However, in stark contrast with the omnipresence of mixing, to date a poor understanding exists of the underlying mechanisms (see Ottino 1990; Harnby, Edwards & Nienow 1992; Aref 1994; King 1998). Far-reaching scientific and social implications are therefore anticipated from expanded knowledge on mixing. The study herein is motivated by this and aims to contribute to the present understanding of mixing via the analysis of tractable case studies prototypical of realistic mixing problems.

The presented investigation is confined to three-dimensional mixing of inert incompressible non-inertial Newtonian fluids with identical material properties. Under these presumptions mixing reduces to the three-dimensional advection of passive tracers – representing minute non-inertial particles and, in the absence of molecular transport, scalars such as heat and mass concentration – in a single-phase non-inertial Newtonian flow. The restriction to non-inertial flow is motivated primarily by the hitherto ill-understood phenomenon of chaotic tracer advection in three-dimensional viscous flows, despite its key role in a wide range of (predominantly industrial) mixing processes. Unlike turbulent flows, where chaotic tracer motion is intrinsic to the stochastic velocity field, in the viscous limit chaotic tracer paths typically coexist with regular flow patterns. This reflects the essential difference between laminar and turbulent mixing and implies that accomplishment of chaotic advection in viscous flows – the key to efficient mixing – is highly non-trivial.

Separation of tracer and flow dynamics in viscous flows suggests that a tracer-based (or Lagrangian) description is essential to the examination of transport phenomena in this flow regime. In a Lagrangian representation tracer motion is described by a dynamical system (see Aref 1994); in the viscous limit, the smooth nature of the flow permits a deterministic analysis of this system with generic dynamical-systems methodology. In this approach the tracer dynamics are investigated in terms of coherent structures in the web of tracer paths (collectively constituting the flow topology). These coherent structures impose geometrical constraints on the tracer motion and thus determine the tracer advection.

For two-dimensional incompressible flows, the Lagrangian system defines a Hamiltonian system (see e.g. Aref 1994). In such systems explicit time-dependence (commonly introduced via time-periodic forcing) is a necessary prerequisite for attaining chaotic advection; two-dimensional steady flows invariably result in non-chaotic tracer dynamics. Numerous studies are dedicated to chaotic advection in two-dimensional time-periodic flows, of which but a few are addressed below. Pioneering work involves the 'blinking-vortex flow' discussed in Aref (1984); an extension to this model is the 'blinking-rotlet flow' (see Meleshko & Aref 1996). The 'classical' two-dimensional laminar mixing flow is found in the lid-driven cavity flow introduced in Chien, Rising & Ottino (1986) and Ottino *et al.* (1988) and server as prototypical configuration in many mixing-related investigations: see e.g. Meleshko (1994), Meleshko & Peters (1996), Franjione, Leong, & Ottino (1989), Ottino, Jana & Chakravarthy (1994) and Kruijt *et al.* (2001). Other two-dimensional bounded flows include the 'journal-bearing flow' (Aref & Balachandar 1986; Muzzio, Swanson & Ottino 1991; Ottino *et al.* 1994), the 'rotor-oscillator flow' (Hackborn, Ulucakli & Yuster 1997) and the 'annular wedged cavity' (Krasnopolskaya *et al.* 1998). Note that Muzzio *et al.* (1991) follow a statistical rather than the customary topological course. Extensive examination of two-dimensional chaotic advection provided a fairly complete picture, leading to the well-known 'fingerprints of chaos' (see e.g. Ottino *et al.* 1994) as indicators of efficient mixing.

Three-dimensional tracer advection, on the other hand, remains a largely unexplored field thus far. Departure from the two-dimensional case has essentially two aspects: first, three-dimensional spaces are of much higher topological complexity than two-dimensional spaces (see Croom 1978), manifesting itself in richer tracer dynamics; and, second, the three-dimensional Lagrangian equations of motion lack the well-defined Hamiltonian structure of their two-dimensional counterpart, hampering a universal approach similar to the two-dimensional case. (Note that an exception to the latter

is three-dimensional steady systems, which, under certain conditions, coincide with time-dependent two-dimensional Hamiltonian systems; see Bajer (1994).) A generic three-dimensional theoretical framework is proposed in Feingold, Kadanoff & Piro (1987), resting on an extension of the concept of action-angle variables known from Hamiltonian mechanics (see Ott 2002) – an essentially topological approach; actions define constants of motion to whose iso-surfaces tracer motion is restricted – to generic three-dimensional dynamical systems (consult Cartwright, Feingold & Piro 1996, for an overview). Further studies involving Hamiltonian concepts are presented in Cheng & Sun (1990), Beigie, Leonard & Wiggins (1994), MacKay (1994) and Mezić & Wiggins (1994). Investigations thus far have exposed several key mechanisms of three-dimensional tracer advection. A well-known feature of three-dimensional systems is e.g. the possibility of chaotic dynamics under steady flow conditions. Examples of such systems are found in Arnol'd (1965), Dombre *et al.* (1986) (the classical ABC flow) and, more recently, in Bajer & Moffatt (1990) and Bajer (1994). The latter tie a phenomenon termed 'trans-adiabatic drifting' to the chaotic behaviour. Note that in time-periodic systems a similar mechanism exists in 'resonance-induced dispersion' (see Cartwright *et al.* 1996). An important theoretical achievement is the three-dimensional analogy to the famous KAM theorem (see Cheng & Sun 1990; Mezić & Wiggins 1994). Numerical studies on (various aspects of) three-dimensional tracer advection are discussed in Ottino (1989), Kusch & Ottino (1992), Ottino *et al.* (1992), Anderson *et al.* (1999), Meleshko *et al.* (1999), Shankar & Deshpande (2000) and Kruijt *et al.* (2001).

Experimental studies on three-dimensional tracer advection are scarce and mainly restricted to the work highlighted below. Seminal work is found in Kusch & Ottino (1992) and Ottino *et al.* (1992), an experimental examination of the partitioned-pipe mixer and eccentric helical annular mixer (prototypical flows introduced in Ottino 1989) by means of flow visualization with fluorescent dye. Chaotic advection in the time-periodic flow in a three-dimensional cylinder, driven by alternate activation of eccentrically rotating endwalls, is investigated in Miles, Nagarajan & Zumbrunnen (1995) via two-dimensional particle tracking velocimetry (PTV) applied to projections of a single three-dimensional tracer path. Laboratory experiments on a steady impeller-driven flow in a cylindrical vessel are described by Fountain, Khakhar & Ottino (1998) and Fountain *et al.* (2000), involving in-plane velocity measurements (PTV) and flow visualization (fluorescent dye).

The present analysis concerns three-dimensional tracer advection by non-inertial flows in the cylindrical configuration introduced in Malyuga *et al.* (2002) and elaborates on their work in a threefold manner. First, the case-specific symmetry-based analysis of the flow topology in Malyuga *et al.* (2002) is reconciled with generic symmetry concepts. This is demonstrated by reconsidering several cases examined in cited work. Second, the study on tracer transport, in Malyuga *et al.* (2002) restricted to individual tracers, is extended to finite-size material objects. Third, several key aspects of flow and tracer dynamics have been subjected to experimental validation.

The paper is organized as follows. Section 2 provides the problem definition. The theoretical framework for the topological approach is outlined in § 3. Laboratory set-up and data-acquisition techniques are presented in § 4. Section 5 contains the numerical flow-topology analysis based on generic symmetry concepts; § 6 contains the numerical study on the transport properties. The laboratory experiments are discussed in § 7. Summary and conclusions are then given in § 8.

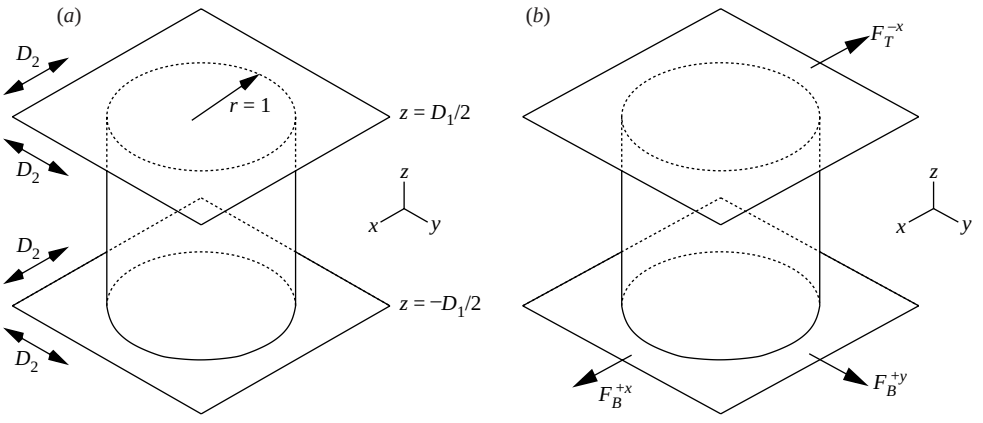

FIGURE 1. (*a*) Non-dimensional problem definition and (*b*) basic forcing steps.

2. Problem definition

2.1. *Tracer kinematics*

The motion of passive tracers is governed by the three-dimensional kinematic vector equation

$$\frac{\mathrm{d}\boldsymbol{x}}{\mathrm{d}t} = \boldsymbol{u}(\boldsymbol{x}, t), \qquad \boldsymbol{x}(0) = \boldsymbol{x}_0, \tag{2.1}$$

describing the temporal evolution of the positions $\boldsymbol{x}$ of tracers released at the position $\boldsymbol{x}_0$ in the flow field $\boldsymbol{u}(\boldsymbol{x}, t)$. The general solution to (2.1), defining a dynamical system, is $\boldsymbol{x}(t) = \boldsymbol{\Phi}_t(\boldsymbol{x}_0)$ and uniquely determines the current position $\boldsymbol{x}$ for given initial tracer position $\boldsymbol{x}_0$. The continuous orbit $\boldsymbol{X}_t(\boldsymbol{x}_0) = \boldsymbol{\Phi}_{t'}(\boldsymbol{x}_0)$, with $t' = [0, t]$, coincides with the Lagrangian trajectory followed by the tracer while propagating from $\boldsymbol{x}_0$ to $\boldsymbol{x}$.

Throughout this paper either steady or time-periodic systems will be considered. For steady systems $\boldsymbol{u} = \boldsymbol{u}(\boldsymbol{x})$ and in consequence the tracer paths coincide with the streamlines of the flow. For time-periodic systems $\boldsymbol{u}(\boldsymbol{x}, t) = \boldsymbol{u}(\boldsymbol{x}, t + T)$, with T the global period, allowing for a reduction of the continuous flow $\boldsymbol{x}(t) = \boldsymbol{\Phi}_t(\boldsymbol{x}_0)$ into the discrete mapping $\boldsymbol{\Phi}_T$. The sequence $\boldsymbol{X}_T(\boldsymbol{x}_0) = [\boldsymbol{x}_0, \boldsymbol{x}_1, \boldsymbol{x}_2, \ldots]$ contains the subsequent tracer positions at the discrete time levels $t = [0, T, 2T, \ldots]$ and forms the temporal Poincaré section of the tracer trajectory $\boldsymbol{X}_t(\boldsymbol{x}_0)$. The present work concerns only n-step time-periodic systems of the form $\boldsymbol{\Phi}_T = \boldsymbol{F}_n\, \boldsymbol{F}_{n-1} \ldots \boldsymbol{F}_1$. The steps $\boldsymbol{F}_i$ form piecewise steady forcing stages with time span T/n, during which one endwall performs a steady translation in a prescribed direction.

2.2. *Flow model*

Restriction to fully non-inertial flows means the fluid motion within each forcing step $\boldsymbol{F}_i$ that is described by the non-dimensional steady Stokes equations

$$\nabla p = \nabla^2 \boldsymbol{u}, \qquad \nabla \cdot \boldsymbol{u} = 0, \tag{2.2}$$

in the non-dimensional cylinder $\mathscr{D} : [r, \theta, z] = [0, 1] \times [0, 2\pi] \times [-D_1/2, D_1/2]$, with $D_1 = H/R$ the aspect ratio of the physical cylinder with radius R and height H. The flow problem is characterized by the non-dimensional parameters D_1 and $D_2 = UT/(nR)$, representing the dimensionless displacement of an endwall during steady forcing ($n = 1$) or one stage of the n-step time-periodic forcing ($n > 1$). Figure 1(*a*) provides a schematic of the non-dimensional problem definition. Here the aspect ratio remains

fixed at $D_1 = 2$, implying that the system is determined entirely by D_2 and the specific forcing protocol.

The relevant time scales are given by the advection time scale $T_a = R/U$ and the forcing time T, related by $T/T_a = nD_2$. The former defines the principal time scale for the tracer dynamics; the dimensionless time t/T_a is therefore forcing-independent and thus facilitates direct comparison of different flow configurations.

2.3. *Flow configurations*

In the following, the forcing steps $\boldsymbol{F}_i$ are one of $(\boldsymbol{F}_B^{+x}, \boldsymbol{F}_T^{-x}, \boldsymbol{F}_B^{+y})$, with the subscripts referring to the top (T) and bottom (B) endwall and the superscripts indicating the translation direction (see figure 1*b*). Geometrical symmetries and stepwise-steady flow imply the basic forcings (and underlying velocity fields) are related via $\boldsymbol{F}_B^{+y} = S_{\pi/2}(\boldsymbol{F}_B^{+x})$ and $\boldsymbol{F}_T^{-x} = S_x S_z(\boldsymbol{F}_B^{+x})$, with the operators $S_{\pi/2}$, S_x and S_z accomplishing $\pi/2$ rotation about the z-axis and reflection about the plane $x = 0$ and $z = 0$, respectively. This suggests the forcing protocols can all be expressed in terms of $\boldsymbol{F}_B^{+x}$, suggesting this as the fundamental building block of the configurations considered hereafter. For forcing $\boldsymbol{F}_B^{+x}$ a semi-analytical solution to (2.2) is presented in Shankar (1997) and Meleshko, Malyuga & Gomilko (2000).

This paper considers four forcing protocols, namely

$$\boldsymbol{\Phi}_t^S = \boldsymbol{F}_B^{+x}, \quad \boldsymbol{\Phi}_T^A = \boldsymbol{F}_B^{+y}\boldsymbol{F}_B^{+x}, \quad \boldsymbol{\Phi}_T^B = \boldsymbol{F}_T^{-x}\boldsymbol{F}_B^{+x}, \quad \boldsymbol{\Phi}_T^C = \boldsymbol{F}_B^{+y}\boldsymbol{F}_T^{-x}\boldsymbol{F}_B^{+x}, \tag{2.3}$$

comprising one steady protocol ($\boldsymbol{\Phi}_t^S$) and three time-periodic protocols ($\boldsymbol{\Phi}_T^{A,B,C}$). Note that these readily connect with the configurations studied in Malyuga *et al.* (2002) upon exchanging top and bottom walls in (2.3).

3. Theoretical setting: the concept of flow topology

3.1. *Coherent structures*

The flow topology is formed by the collection of coherent structures embedded in the web of tracer paths. The flow topology imposes geometrical constraints on the tracer motion and thus dictates the advection characteristics of a given flow. For both steady and time-periodic systems three categories of coherent structures can be envisioned: (i) periodic points and lines; (ii) invariant manifolds attached to periodic points and lines; (iii) generic closed invariant manifolds (see e.g. Guckenheimer & Holmes 1983; Feingold *et al.* 1988). Note that stagnation points and lines readily qualify as periodic points and lines.

Coherent structures are, notwithstanding the chaotic – and thus inherently unpredictable – nature of individual tracers, structurally stable and thereby robustly detectable in chaotic systems. The flow topology represents the 'order within disorder' and its identification therefore forms the key to understanding of chaotic advection in fluid-dynamical systems.

Brouwer's fixed-point theorem states that any continuous mapping of a convex space† onto itself has at least one fixed (or periodic) point (see Brouwer 1911). This fundamental property projects periodic points and associated invariant manifolds

† A space is termed convex if for any pair of points within the space, any point on the line joining them is also within the space. The present cylindrical domain is such a convex space.

as the most essential entities in the flow topology.† Periodic points and lines fall within one of the following categories: node-type and focus-type periodic points and elliptic, hyperbolic and parabolic periodic lines (see Malyuga *et al.* 2002). In steady systems, periodic points describe closed streamlines on which any constituent point is periodic; such closed streamlines thus form uniform-type (i.e. fully elliptic, hyperbolic or parabolic) periodic lines (see Ott 2002). Time-periodic systems allow for periodic lines with elliptic and hyperbolic segments (see Malyuga *et al.* 2002). Note that for steady systems an alternative classification for stagnation points is found in Chong, Perry & Cantwell (1990), which can be shown to connect consistently with the classification of Malyuga *et al.* (2002).

Several coherent structures associated with periodic points and lines can be distinguished. Isolated periodic points and hyperbolic elliptic lines imply pairs of stable (W^S) and unstable (W^U) manifolds, arising as surface–curve pairs ($W_{2D}^{S,U}, W_{1D}^{U,S}$) for points and as surface–surface pairs ($W_{2D}^{S,U}, W_{2D}^{U,S}$) for lines. The manifolds can, depending on their interaction, either obstruct or promote chaotic tracer transport. Elliptic lines form the centre of families of so-called elliptic tubes that seal off the enclosed region and thus act as transport barriers. Parabolic lines are devoid of associated coherent structures and indicate (inherently non-chaotic) shear flow.

The nature of the tracer dynamics is intimately related to the manifold interaction $W^s - W^u$. Two kinds of interaction scenarios can be distinguished: (i) homoclinic (W^s, W^u belong to one point/line) or heteroclinic (W^s, W^u belong to different points/lines) interaction; (ii) smooth connection or transversal intersecting of stable with unstable manifolds. Hetero/homoclinic smooth connections imply closed orbits and thus non-chaotic tracer dynamics. Hetero/homoclinic transversal manifold interaction, on the other hand, forms one of the established 'fingerprints of chaos' (see Ottino *et al.* 1994).

In steady systems the manifolds coincide with streamlines and stream surfaces, suggesting that $W_{1D} - W_{2D}$ intersections are identified with stagnation points and thus are disqualified as legitimate transversal interaction. In consequence, transversal interaction is possible only between two-dimensional manifolds, namely as heteroclinic point–point, heteroclinic point–line, homoclinic line–line and heteroclinic line–line interaction (see Abraham & Shaw 1982). In time-periodic systems such restrictions are absent and, hence, virtually boundless combinations are conceivable, leaving manifold dynamics in three-dimensional time-periodic flows an area largely unexplored so far.‡ Note that periodic lines suggest (locally) two-dimensional tracer dynamics (see Malyuga *et al.* 2002).

3.2. *Symmetries*

Symmetries in the flow field manifest themselves as symmetries in the tracer trajectories and can thereby facilitate identification of coherent structures. For the purpose of this study a brief overview, largely based on the work presented in Franjione *et al.* (1989) and Ottino *et al.* (1992), is given below.

In the present framework two kinds of symmetries are of interest, namely

$$\boldsymbol{\Phi}_\tau = S\boldsymbol{\Phi}_\tau S^{-1}, \qquad \boldsymbol{\Phi}_\tau = S\boldsymbol{\Phi}_\tau^{-1} S^{-1}, \tag{3.1}$$

† "What makes periodic solutions so valuable is that they offer the only opening through which we might try to penetrate the fortress which has the reputation of being impregnable", according to Poincaré (1892).

‡ Transversal $W_{1D}^s - W_{1D}^u$ interaction is unlikely, however, following the transversality theorem (see Guckenheimer & Holmes 1983).

with $\tau = t$ and $\tau = T$ for steady and time-periodic systems, respectively, reflecting ordinary and time-reversal symmetry, respectively, in the flow $\boldsymbol{\Phi}_\tau$ about the fixed manifold of symmetry I_S (given by $S(I_S) = I_S$). For time-periodic systems $\boldsymbol{\Phi}_T = \boldsymbol{F}_n \boldsymbol{F}_{n-1} \ldots \boldsymbol{F}_1$ a second class of symmetries exists:

$$\boldsymbol{F}_i = S\boldsymbol{F}_j S^{-1}, \qquad \boldsymbol{F}_i = S\boldsymbol{F}_j^{-1} S^{-1}, \tag{3.2}$$

reflecting symmetries between the individual stages of the forcing sequence. Note that for $i = j$ relation (3.2) denotes self-symmetry within one single step $\boldsymbol{F}_i$. For the present multistep systems, global symmetries (3.1) are derived directly from (3.2). Furthermore, a distinction must be made between reflectional and non-reflectional symmetries on the following topological grounds. For the former, I_S defines the surface of reflection, which physically divides the domain – and thereby flow topology – into two inter-related sections. For the latter, I_S is identified with either a curve or a single point and in consequence such spatial subdivision is absent. Note that for reflectional symmetries $S^2 = I$ and thus $S^{-1} = S$.

Application of property (3.1) to coherent structures L gives $\boldsymbol{\Phi}_\tau^{\pm 1} S(L) = S(L)$ and implies that they emerge as pairs $[L, S(L)]$. Introducing L_I to denote (segments of) coherent structures located on I_S then gives

$$[L_I, L, S(L)], \tag{3.3}$$

as the fundamental arrangement of coherent structures in symmetric systems, suggesting the flow topology is determined entirely by $[L_I, L]$. The immediate implication for systems with (time-reversal) reflectional symmetries is that scanning of only one of the two subdomains separated by I_S is sufficient to identify $[L_I, L]$. (Note that an equivalent reduction is lacking for non-reflectional symmetries; clearly defined subdomains are absent in that case.) Further universal manifestations of (reflectional) symmetries are given below.

For ordinary reflectional symmetries, I_S is impenetrable and thus acts as a 'virtual wall', physically separating the flows on each side. In the case of time-reversal reflectional symmetry, periodic structures on I_S (denoted P_I) are defined by intersections

$$P_I = \mathscr{I}_S \cap \boldsymbol{\Phi}_\tau(\mathscr{I}_S), \tag{3.4}$$

with $\mathscr{I}_S$ the material surface released at I_S. Because $\mathscr{I}_S$ and $\boldsymbol{\Phi}_\tau(\mathscr{I}_S)$ are both surfaces, the intersection P_I defines invariant curves, for steady and time-periodic flows corresponding to stagnation and period-k lines, respectively. Bounded systems with the symmetry mentioned above invariably accommodate such lines (see Speetjens 2001). The time-reversibility underlying S relates the members of the manifold pair (W_{2D}^u, W_{2D}^s) of hyperbolic (segments of) P_I via $W_{2D}^s = S(W_{2D}^u)$; for periodic structures P off I_S, by virtue of (3.3) emerging in pairs $[P, S(P)]$, one arrives in a similar manner at $W_P^{u,s} = S(W_{S(P)}^{s,u})$.

For systems encompassing two time-reversal reflectional symmetries (termed 'double-symmetric'), i.e. S_1 and S_2, one symmetry, say S_2, forms a conjugate pair (S_2, S_2'), with $S_2' = S_1 S_2 S_1$ and $I_2' = S_1(I_2)$. Period-1 lines P are given in such systems by the intersections of the conjugate surfaces, $P = \mathscr{I}_2 \cap \mathscr{I}_2'$ (see Ottino *et al.* (1994) for the two-dimensional counterpart), or, in terms of (3.3), by $P = [P_1, P_2, S_1(P_2)]$, with $P_{1,2}$ conforming to (3.4) for $\tau = T$. Manifold pairs, if present, satisfy $W_{P_1}^s = S_1(W_{P_1}^u)$, $W_{P_2}^s = S_2(W_{P_2}^u)$ and $W_{P_2'}^{u,s} = S_1(W_{P_2}^{s,u})$, with $P_2' = S_1(P_2)$.

Furthermore, flow configurations generally allow for case-specific symmetry exploitation, including any symmetry disclosed for a given problem. An instructive example on this is found in the tailor-made search algorithm for periodic points in

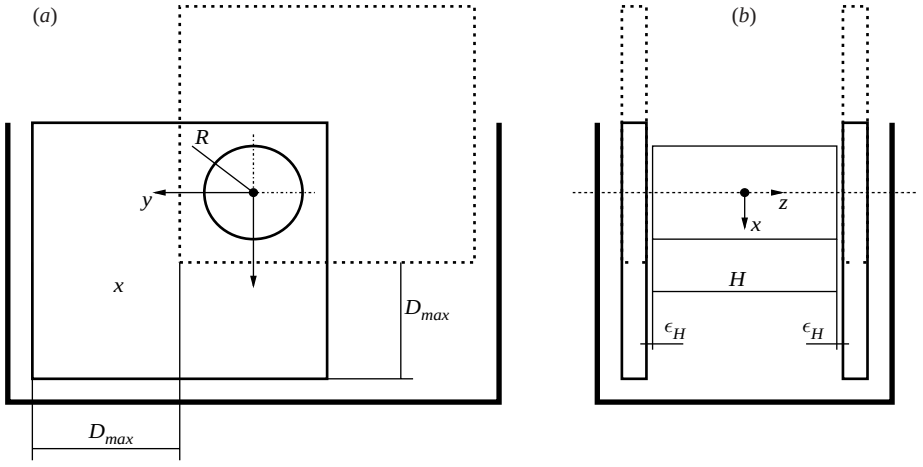

FIGURE 2. Schematic of the laboratory set-up. The solid and dashed squares in (*a*) reflect the maximum horizontal/vertical displacement (distance D_{max}) of either endwall.

the classical two-dimensional lid-driven cavity, as presented in Meleshko & Peters (1996).

4. Experimental techniques

4.1. *Apparatus*

The laboratory set-up consists of a container filled with silicon oil (type AK2000 by Wacker-Chemie GMBH, Munich, Germany) into which the cylinder is submerged; the endwalls are mounted on support structures and lowered into the fluid. In-plane motion of the endwalls is accomplished via a computer-controlled motion-control system by which both the displacement $D \leqslant D_{max}$ (the upper bound results from the finite-size endwalls) and velocity $U \leqslant U_{max}$ are set and monitored, permitting optimal reproducibility of the forcing conditions. Container, cylinder and endwalls are fabricated of translucent Perspex for maximum optical accessibility. (Note that D_{max} permits long-term experiments only for forcing protocols with net zero-displacement during one period.) A schematic of the apparatus, with specifications $H = 70\,\text{mm}$, $R = 35\,\text{mm}$, $\epsilon_H = 1\,\text{mm}$, $\nu = 2000\,\text{mm}^2\,\text{s}^{-1}$, $D_{max} = 210\,\text{mm}$ and $U_{max} = 20\,\text{mm}\,\text{s}^{-1}$, is given in figure 2. (Note that the cylinder has for practical reasons been put on its side in the laboratory set-up.) The relative gap between endwalls and cylinder is $\epsilon_H/H = 1/70 \ll 1$ and is considered negligible. The aspect ratio and maximum non-dimensional displacement are $D_1 = 2$ and $D_{2,max} = 6$, respectively. In this paper, U is set such that $Re = UR/\nu = 0.06$, which allows neglect of inertial effects, implying the laboratory conditions are consistent with the problem definition of § 2.

4.2. *Flow visualization and flow measurement*

Material volumes ('blobs') are labelled via injection of dyed silicon oil (dye stuffs: Sudan Blau II and Sudan Orange 183 by BASF AG, Ludwigshafen, Germany) for visualization of the tracer transport. The blobs are photographed at subsequent stages in the forcing cycle for qualitative comparison with numerical predictions. Laboratory observations determined the dye–oil solution to be inert and fully miscible and mass diffusion proved insignificant within the typical time span of an experiment (Schmidt number $Sc = \nu/\kappa \sim O(1500)$), thus meaning that the blobs qualify as passive tracers.

Quantitative data on velocity field and tracer paths are obtained by means of particle tracking velocimetry (PTV). The method in essence comprises an image-processing algorithm by which the quantities are deduced from video recordings of the time evolution of minute particles seeded in the fluid. Prior to measuring sessions, a three-dimensional reference grid is recorded, enabling data-translation from pixel to physical coordinates. In the three-dimensional case the imagery is procured via a three-camera configuration with non-coinciding viewpoints (see Kieft *et al.* 2002; Schreel, van der Plas & Kieft (2000)).

High-resolution cameras (1018×1019 pixels 10-bit camera model ES 1.0 by Roper Scientific, San Diego, USA) were positioned in a triangular arrangement facing the bottom endwall at an angle $\alpha \simeq 9^\circ$ with the cylinder axis, a trade-off between optimal performance ($\alpha \simeq 20^\circ$, see Kieft *et al.* 2002) and maximum optical accessibility ($\alpha \to 0^\circ$). Transformation of the measured velocity field from the set of N unstructured measuring points $\boldsymbol{x}$ to a structured grid $\boldsymbol{\epsilon}$ is established via the kernel-based interpolation scheme $\overline{\boldsymbol{u}}(\boldsymbol{\epsilon}, t) = \sum_i^N G(\boldsymbol{x}_i - \boldsymbol{\epsilon}, \sigma)\boldsymbol{u}(\boldsymbol{x}_i, t) / \sum_i^N G(\boldsymbol{x}_i - \boldsymbol{\epsilon}, \sigma)$, with $G(\boldsymbol{x}, \sigma) = \mathscr{G}(x, \sigma)\,\mathscr{G}(y, \sigma)\mathscr{G}(z, \sigma)$ and $\mathscr{G}(x, \sigma)$ the well-known Gaussian function. An optimum window size σ is found to be $\sigma = 1.24\delta/\sqrt{2} \approx 0.88\delta$, with $\delta = \sqrt[3]{3V/4\pi N}$ the mean particle separation in the three-dimensional domain of volume $V = \pi H R^2$ and N as before, based on the procedure proposed in Agüi & Jiménez (1987).

5. Numerical analysis: flow topology

5.1. *Steady flow*

The semi-analytical solution of (2.2) under the steady forcing in (2.3) is of the form

$$u_r(\boldsymbol{x}) = \omega_r(r, z)\cos\theta, \qquad u_\theta(\boldsymbol{x}) = \omega_\theta(r, z)\sin\theta, \qquad u_z(\boldsymbol{x}) = \omega_z(r, z)\cos\theta, \quad (5.1)$$

defining a flow field with streamlines $\boldsymbol{X}_t(\boldsymbol{x}_0)$ symmetric about the plane $y = 0$ and self-symmetric about $x = 0$ (see Meleshko *et al.* 2000). In terms of the symmetry operators introduced in § 3.2, the flow satisfies

$$\boldsymbol{\Phi}_t = S_y \boldsymbol{\Phi}_t S_y, \qquad \boldsymbol{\Phi}_t = S_x \boldsymbol{\Phi}_t^{-1} S_x, \quad (5.2)$$

signifying an ordinary (S_y) and time-reversal (S_x) reflectional symmetry about the planes $y = 0$ (I_y) and $x = 0$ (I_x), respectively. According to § 3.2, properties (5.2) dictate that coherent structures are symmetric about both I_x and I_y. Moreover, the presence of S_x implies a stagnation line in the plane I_x. This agrees with Shankar (1997), in which an elliptic stagnation line is reported in I_x and symmetric about I_y. Moreover, two isolated focus-type stagnation points are found, located in I_y near the upper-right and upper-left corners and symmetrically arranged about I_x, exhibiting heteroclinic point-point interaction via the smooth connections $W^s_{1D} - W^u_{1D}$ and $W^s_{2D} - W^u_{2D}$. The tracer paths outside the interacting manifolds invariably consist of closed streamlines – following § 3.1 identified with periodic lines – centred on the stagnation line. The presence of a dense set of such periodic lines implies that they are parabolic, in turn implying shear-like fluid flow – and thus non-chaotic tracer dynamics.

Closed streamlines suggest the existence of two constants of motion $F(\boldsymbol{x})$, which are governed by $\boldsymbol{u} \cdot \nabla F = 0$ and, consistent with (5.1), can be shown to be of the form

$$F_1(\boldsymbol{x}) = f_1(r, z), \qquad F_2(\boldsymbol{x}) = f_2(r, z)\sin\theta, \quad (5.3)$$

where an analytical expression for F_1 is provided in Malyuga *et al.* (2002). Tracers released at $\boldsymbol{x}_0$ adhere to pairs of level surfaces $F_{1,2}(\boldsymbol{x}_0) = F_{1,2}(\boldsymbol{x})$, meaning that streamlines are defined by intersections of level surfaces of $F_{1,2}$ (see Bajer 1994).

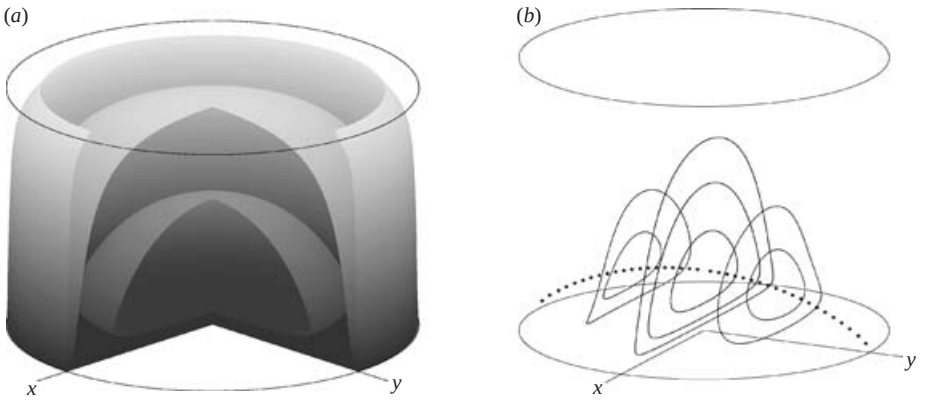

FIGURE 3. Coherent structures in the steady flow: concentric level surfaces of F_1 (closed surfaces in a) inside the separatrix F_1' (surface ending on top wall in a); 'primary-eddy region' consisting of elliptic stagnation line (dotted curve) and encircling parabolic lines (b).

The anti-symmetry of F_2 about I_y means that the level surface $F_2 = 0$ coincides with I_y; the intersections of $F_2 = 0$ with the level surfaces of F_1 then define the streamline portrait in I_y. Conversely, the latter implies that the axi-symmetric level surfaces of F_1 are identified with the surfaces of revolution of the streamlines in I_y. This, in turn, means that the projection of arbitrary three-dimensional streamlines onto the (r, z)-plane coincides with the streamline pattern in I_y.

An important ramification of the above is that it, in the present context, nullifies the effect of the foci upon the tracer dynamics. In I_y the zone of influence of the foci sits between a separation streamline ending on the top wall and the boundary (see Shankar 1997); in three-dimensions this separation streamline, by virtue of the above symmetry property, corresponds to an axi-symmetric separatrix F_1' within which the level surfaces of F_1 constitute a family of concentric sphere-like objects (see figure 3a). The region outside this separatrix – defining the three-dimensional zone of influence of the foci – forms but a thin boundary layer in which fluid motion is negligible relative to the interior of F_1'. This suggests that the foci are insignificant for the advection characteristics and thus leaves the stagnation line and encircling parabolic lines (merging into the family of elliptic tubes that defines the 'primary-eddy region' in Shankar 1997) as relevant coherent structures (see figure 3b). The level surfaces of F_2 (not shown) define a family of parallel vertical surfaces symmetrically arranged about I_y.

5.2. *Time-periodic flows*

5.2.1. *Forcing protocol A*

The symmetries of the steps in forcing protocol A derive from (5.2) and collapse onto

$$\left.\begin{array}{llll} \boldsymbol{F}_1 = S_y \boldsymbol{F}_1 S_y, & \boldsymbol{F}_1 = S_x \boldsymbol{F}_1^{-1} S_x, & \boldsymbol{F}_2 = S_x \boldsymbol{F}_2 S_x, & \boldsymbol{F}_2 = S_y \boldsymbol{F}_2^{-1} S_y, \\ \boldsymbol{F}_1 = S_1 \boldsymbol{F}_2 S_1, & \boldsymbol{F}_1 = S_2 \boldsymbol{F}_2^{-1} S_2, & \boldsymbol{F}_2 = S_1 \boldsymbol{F}_1 S_1, & \boldsymbol{F}_2 = S_2 \boldsymbol{F}_1^{-1} S_2, \end{array}\right\} \tag{5.4}$$

with $S_1 : (x, y, z) \rightarrow (y, x, z)$ and $S_2 : (x, y, z) \rightarrow (-y, -x, z)$ establishing reflection about the planes $y = x$ and $y = -x$, respectively, and $S_{x,y}$ as defined before. The symmetries are related through $S_x = S_1 S_y S_1$ and $S_2 = S_y S_1 S_y$, meaning that the system accommodates only two independent symmetries, namely S_y and S_1. Symmetries (5.4)

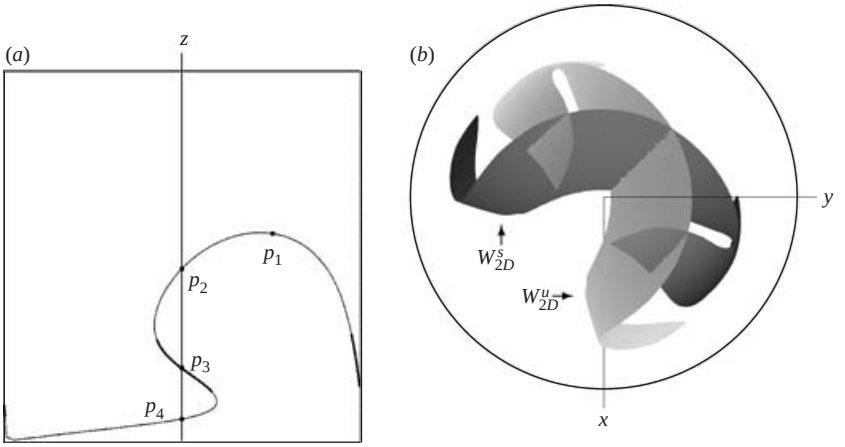

FIGURE 4. Period-1 line in the plane $y=-x$ (a; viewed in the negative x-direction) and manifold pair (W^s_{2D}, W^u_{2D}) (b; viewed from above) for protocol A at $D_2=5$.

become via $\boldsymbol{F}_2\boldsymbol{F}_1 = S_2\boldsymbol{F}_1^{-1}S_2\,S_2\boldsymbol{F}_2^{-1}S_2 = S_2(\boldsymbol{F}_2\boldsymbol{F}_1)^{-1}S_2$ the time-reversal reflectional symmetry S_2, with the plane $y=-x$ as fixed manifold of symmetry I_2. Moreover, an ordinary non-reflectional symmetry is found through $\boldsymbol{F}_2\boldsymbol{F}_1 = S_1\boldsymbol{F}_1S_1S_1\boldsymbol{F}_2S_1 = S_1\boldsymbol{F}_1\boldsymbol{F}_2\boldsymbol{F}_1\boldsymbol{F}_1^{-1}S_1 = \widetilde{S}(\boldsymbol{F}_2\boldsymbol{F}_1)\widetilde{S}^{-1}$, with $\widetilde{S}=S_1\boldsymbol{F}_1$ and $\widetilde{S}^2=\boldsymbol{F}_2\boldsymbol{F}_1=\boldsymbol{\Phi}_T^A$. The independent symmetries S_y and S_1 in (5.4) thus translate into the global symmetry relations

$$\boldsymbol{\Phi}_T = S_2\boldsymbol{\Phi}_T^{-1}S_2, \qquad \boldsymbol{\Phi}_T = \widetilde{S}\boldsymbol{\Phi}_T\widetilde{S}, \tag{5.5}$$

with S_2 and $\widetilde{S}$ as before.

Symmetry S_2 implies, first, that scanning of either side of I_2 suffices for full identification of the flow topology and, second, that I_2 hosts a period-1 line given by relation (3.4). Figure 4(a) displays the period-1 line for $D_2=5$, viewing the plane I_2 in the negative x-direction, where thick and thin lines indicate elliptic and hyperbolic segments, respectively. The period-1 line meets $L=\widetilde{S}(L)$ and intersects with the cylinder axis (p_3 in panel a) at the stagnation point $\boldsymbol{x}_0 = L_x \cap L_y$, with L_x and $L_y = S_{\pi/2}(L_x)$ the stagnation lines associated with $\boldsymbol{F}_B^{+x}$ (see figure 3) and $\boldsymbol{F}_B^{+y}$, respectively. The coincidence of the stagnation point – which sits at the same position for any D_2 – with the period-1 line reflects the analogy between the stagnation point and period-1 points indicated in § 3.1. Period-1 points and lines outside I_2 are non-existent (see Malyuga *et al.* 2002).

The part of the two-dimensional unstable manifold W^u_{2D} connected to the segment $[p_1, p_2]$ of the period-1 line is identified with the technique described in Malyuga *et al.* (2002). Following § 3.2, the time-reversal reflectional symmetry S_2 implies $W^s_{2D} = S_2(W^u_{2D})$, meaning that isolation of the unstable manifold W^u_{2D} is sufficient for finding the manifold pair (W^u_{2D}, W^s_{2D}). Figure 4(b) shows a portion of the latter as seen from above (manifolds are infinitely long; thus here only part of them is displayed). The intersection $W^s_{2D} \cap W^u_{2D}$ in I_2 corresponds to the segment $[p_1, p_2]$ of the period-1 line; the intersections off I_2 define transverse homoclinic intersections and thereby suggest chaotic dynamics, albeit of an essentially two-dimensional nature.

The previous constant of motion F_1 is, due to its axisymmetry, invariant under changes in bottom-wall translation direction, meaning that F_1 is preserved for protocol A. This restricts tracers to effectively two-dimensional motion on the corresponding level surfaces shown in figure 3(a) and suggests that the above period-1 line consists

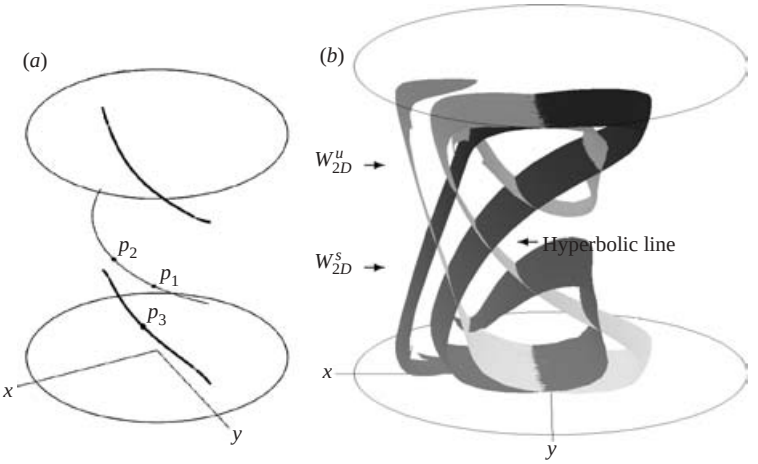

FIGURE 5. Flow topology for protocol B at $D_2 = 5$. (a) Period-1 lines, (b) manifold pair.

of period-1 points each associated with a given level surface of F_1. The invariable existence of these period-1 points – and thus the period-1 line – follows from Brouwer's fixed-point theorem (see § 3.1).† This property extends to any time-periodic forcing protocol involving only one endwall and implies that this flow class always hosts at least one period-1 line.

5.2.2. *Forcing protocol B*

The symmetry properties for protocol B follow from (5.2) and are

$$\boldsymbol{F}_{1,2} = S_x \boldsymbol{F}_{1,2}^{-1} S_x, \qquad \boldsymbol{F}_1 = S_z \boldsymbol{F}_2^{-1} S_z, \qquad \boldsymbol{F}_2 = S_z \boldsymbol{F}_1^{-1} S_z, \qquad \boldsymbol{F}_{1,2} = S_y \boldsymbol{F}_{1,2} S_y, \quad (5.6)$$

with $S_{x,y,z}$ as before. Time-reversal reflectional symmetry is identified through $\boldsymbol{F}_2\boldsymbol{F}_1 = (S_z\boldsymbol{F}_1^{-1}S_z)(S_z\boldsymbol{F}_2^{-1}S_z) = S_z(\boldsymbol{F}_2\boldsymbol{F}_1)^{-1}S_z$ with I_z the plane $z = 0$. The self-symmetry S_x co-exists with a second time-reversal reflectional symmetry S_2, following from $\boldsymbol{F}_2\boldsymbol{F}_1 = (S_x\boldsymbol{F}_2^{-1}S_x)(S_x\boldsymbol{F}_1^{-1}S_x) = (S_x\boldsymbol{F}_1)\boldsymbol{F}_1^{-1}\boldsymbol{F}_2^{-1}(\boldsymbol{F}_1^{-1}S_x) = S_2(\boldsymbol{F}_2\boldsymbol{F}_1)^{-1}S_2$, with $S_2 = S_x\boldsymbol{F}_1 = S_2^{-1}$ and $I_2 = \boldsymbol{F}_1^{-1/2}(I_x)$ and conjugates $S_2' = S_zS_2S_z$ and $I_2' = S_z(I_2)$. This makes protocol B a double-symmetric system, in which period-1 lines are determined entirely by the intersections $P = \mathscr{I}_2 \cap \mathscr{I}_2'$ (see § 3.2). Furthermore, an ordinary reflectional symmetry is found in $\boldsymbol{\Phi}_T = S_y\boldsymbol{\Phi}_T S_y$.

Figure 5(a) displays the period-1 lines for $D_2 = 5$, comprising one hyperbolic line sitting in I_z and two elliptic lines symmetrically arranged about I_z. The part of the manifold pair (W^s_{2D}, W^u_{2D}) attached to the segment $[p_1, p_2]$ of the hyperbolic line is displayed in figure 5(b). The stable and unstable manifold are related via $W^s_{2D} = S_z(W^u_{2D})$ and are symmetric about $y = 0$. Transversal homoclinic interaction occurs between the two-dimensional manifolds, similar to protocol A, signifying two-dimensional chaotic tracer dynamics. Note that the essentially two-dimensional nature of flows with periodic lines is particularly apparent for protocol B. Both uniform-type periodic lines and the nearly absent lateral stretching of the manifolds are manifestations of this characteristic.

† The essential premise of convexity is fulfilled by the level surfaces of F_1.

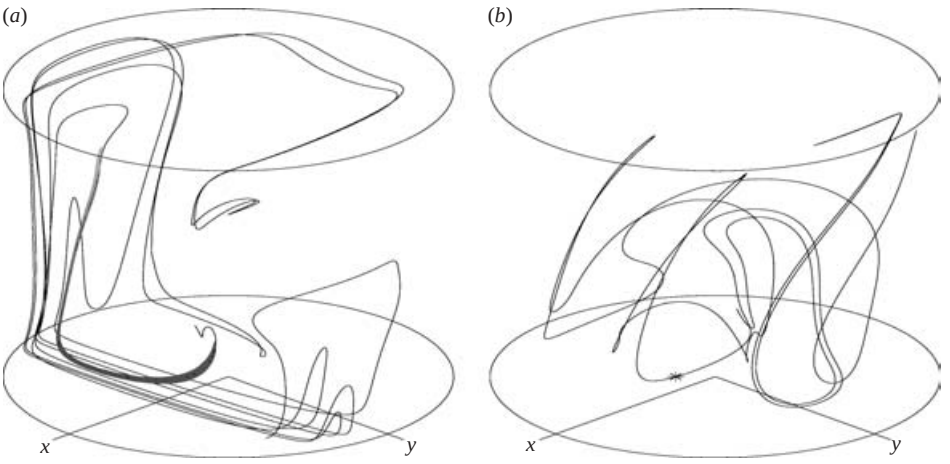

FIGURE 6. Protocol C: manifolds of lower periodic point ($D_2 = 5$). (a) W^u_{2D}, (b) W^s_{1D}.

5.2.3. *Forcing protocol C*

Protocol C encompasses three steps, relating to protocols A and B via $\boldsymbol{F}^C_1 = \boldsymbol{F}^A_1 = \boldsymbol{F}^B_1$, $\boldsymbol{F}^C_2 = \boldsymbol{F}^B_2$ and $\boldsymbol{F}^C_3 = \boldsymbol{F}^A_2$, with the superscripts indicating the protocol in question. Symmetry analysis, taking into account properties (5.4) and (5.6), reveals protocol C to be devoid of global symmetries such as those found for protocols A and B. Periodic structures for protocol C are therefore isolated with the case-specific symmetry-based search algorithm proposed in Malyuga *et al.* (2002).

Two isolated node-type periodic points are found for $D_2 = 5$, one near the origin and one near the bottom wall, with associated manifold pairs (W^u_{2D}, W^s_{1D}). Stretching rates are roughly five times as high for the latter periodic point compared to the former, however (see Malyuga *et al.* 2002), implying that the global advection properties are governed primarily by the periodic point near the bottom wall. The discussion hereafter therefore concentrates on the latter. Figure 6(a) shows W^u_{2D} corresponding to that point, the filament-like shape of which signifies a dominant stretching direction within W^u_{2D}. This is consistent with the intraplanar stretching-rate ratio $|\lambda_I/\lambda_{II}| = 3.9$, with $\lambda_{I,II}$ the stretching rates along the two principal deformation axes in W^u_{2D}, which significantly differs from unity (see Malyuga *et al.* 2002). The one-dimensional stable manifold W^s_{1D} is depicted in figure 6(b), with the star indicating the location of the periodic point.

The part of the flow topology decisive for the tracer transport thus consists of the entities displayed in figure 6. Its intricate and essentially three-dimensional extent sets the topology of protocol C apart from the effectively two-dimensional flow topologies of protocols A and B, reflecting the fundamental difference between systems with periodic lines and systems with isolated periodic points. Furthermore, for the former, transversal manifold interaction is a necessary condition for chaotic dynamics and as such serves as the well-established 'fingerprint of chaos'. For protocol C, on the other hand, three-dimensional chaotic advection is observed without finding manifold interaction of any kind, suggesting that in three-dimensional systems the mere existence of isolated periodic points is a sufficient indicator of three-dimensional chaos. Note that smooth connection can be ruled out on grounds of the properties of the manifold pairs: here one finds (W^u_{2D}, W^s_{1D}) for both periodic points; the interaction mentioned, on the other hand, requires (W^u_{2D}, W^s_{1D}) for one point and (W^u_{1D}, W^s_{2D}) for

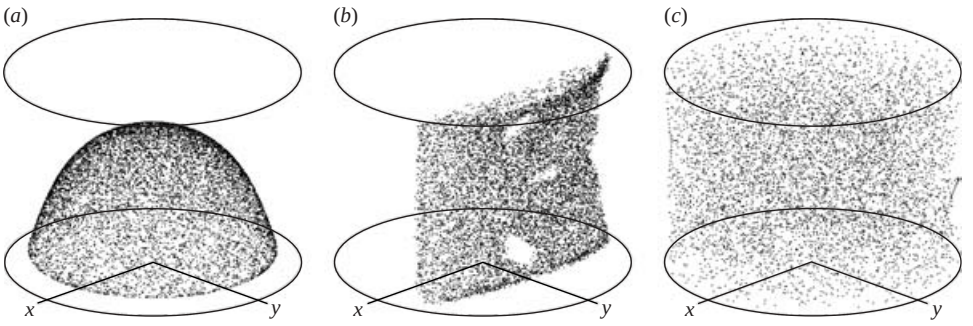

FIGURE 7. Long-term tracer dispersion for the time-periodic forcing protocols ($D_2 = 5$). Protocols A, B and protocol C are tracked for 10 000 and 6667 periods, respectively, and cover a total time span $t_{tot}/T_a = 1 \times 10^5$. ($a$) Protocol A, (b) B, (c) C.

the other in order to form smooth connections $W^u_{2D} - W^s_{2D}$ and $W^u_{1D} - W^s_{1D}$. Whether or not this automatically implies transversal interaction, as in the periodic-line case, remains to be seen, however.

6. Numerical analysis: advection characteristics

The link between flow topology and tracer transport is investigated by determining the advection characteristics of individual tracers and finite-size material objects (surfaces and volumes), released at strategic locations in the flow. Both approaches are complementary in that monitoring of tracers and objects provides insight into the long-term and short-term behaviour, respectively, of a given system. Both tracers and objects are examined in terms of Poincaré sections (see § 2.1); for objects their interface with the ambient fluid is tracked with the algorithm proposed in Malyuga *et al.* (2002).

6.1. *Individual tracers*

In the steady-forcing case tracers migrate on the closed streamlines displayed in figure 3 and, hence, Poincaré sections $\boldsymbol{X}_T(\boldsymbol{x}_0)$ of individual tracers coincide with one such streamline. Advection is restricted by two constants of motion, implying effectively one-dimensional motion and thus inherently non-chaotic tracer dynamics.

For protocols A and B one tracer is released on W^u_{2D} at a minute distance from the periodic line; for protocol C the same is done for the dominant stretching direction in W^u_{2D}. Protocols A, B and protocol C are tracked for 10 000 and 6667 periods respectively with $D_2 = 5$ and thus cover a time span $t_{tot}/T_a = 1 \times 10^5$. Figure 7($a$) displays the Poincaré section for protocol A and reveals essentially two-dimensional motion in that the tracer, though wandering chaotically, is confined to one level surface of F_1. For protocol B similar behaviour is found in that tracers are restricted to thin layers of approximately constant y, hosting quasi-two-dimensional chaotic dynamics (see figure 7b). Note that the white patches in the cloud of subsequent tracer positions in figure 7(b) indicate the location of the tubes centred on the elliptic lines. Essentially three-dimensional chaotic advection is found only for protocol C, for which one tracer visits the entire flow domain (see figure 7c), signifying that transport barriers are non-existent.

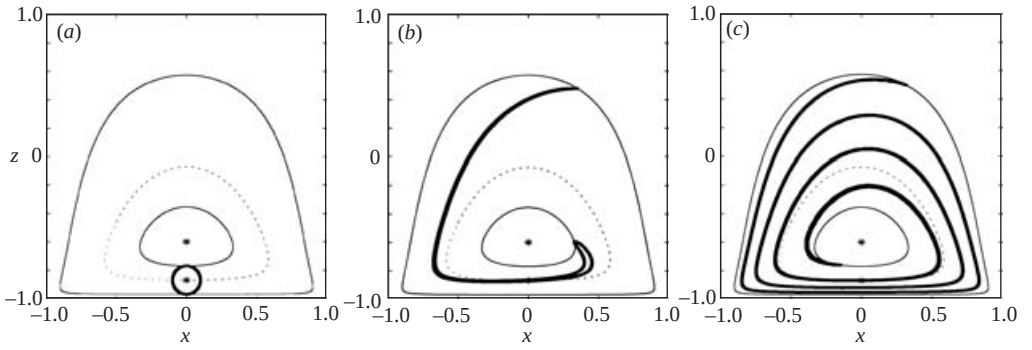

FIGURE 8. Advection of a material surface (thick line) in the steady flow ($T/T_a = 10$). (*a*) $t = 0$, (*b*) $t = T$, (*c*) $t = 4T$.

6.2. *Finite-size material objects*

For the steady forcing case, the dynamics of finite-size material objects are examined in terms of the discrete mapping $\boldsymbol{\Phi}_T^S$ deriving from $\boldsymbol{\Phi}_t^S$, with T the period of protocols A and B. Tracer motion is confined to closed streamlines in level surfaces of F_2 and, therefore, concentrating on one such level surface, say $F_2 = 0$ (plane $y = 0$), provides sufficient information on the global advection characteristics. In the mapping, the elliptic stagnation line then emerges as an elliptic period-1 point – with associated island defined by the encircling closed streamlines (see figure 3*b*) – in the plane $y = 0$. Moreover, the points $p_{2,4}$ in figure 4(*a*) can be shown to share one closed streamline, in the mapping materializing as a parabolic period-1 line in the plane $y = 0$.

Figure 8 shows the temporal evolution of the interface (thick line) of a material disk with radius $r/R = 0.1$ released on p_4 (lower star on the z-axis). The thin solid lines represent the orbits in the elliptic island of p_3 (upper star on the z-axis), along which the poles of the initially circular interface travel. The dotted line delineates the closed trajectory pursued by p_4 in the course of one period. The time-sequence exposes the shear-like deformation of the disk, akin to that of a two-dimensional shear flow, in the annular flow confined by the thin solid lines. This is typical of the advection in any annulus defined by any two closed streamlines in any level surface of F_2 and thereupon advances the steady flow as essentially equivalent to two-dimensional shear flow.

For the time-periodic protocols the advection of material spheres with radius $r/R = 0.1$ is investigated for $D_2 = 5$. For protocol A blobs are placed on the cylinder axis at positions p_3 and p_4 in figure 4(*a*), corresponding to an elliptic and hyperbolic point, respectively, on the periodic line. The evolution of the blobs is shown in figure 9 and reveals dramatic differences in the response of the two objects, despite their initial proximity, to the imposed forcing. The blob on p_3 (elliptic) remains practically undeformed; the blob on p_4 (hyperbolic), in sharp contrast, deforms substantially and gradually wraps itself about the other blob in the course of time. These phenomena can be reconciled with the flow topology of protocol A in that the blob on p_3 is trapped in the elliptic tube centred on the elliptic segment of the periodic line, whereas the blob on p_4 collapses on the unstable manifold W_{2D}^u of the hyperbolic segment of the periodic line (enveloping the mentioned tube) as time progresses. This is in accord with the notion that unstable manifolds in conservative ($\nabla \cdot \boldsymbol{u} = 0$) flows are analogous to attractors in dissipative ($\nabla \cdot \boldsymbol{u} < 0$) flows (see Beigie *et al.* 1994). Furthermore, the constant of motion F_1 restricts the freedom of movement of the blob on p_4 to the three-dimensional annulus bounded by the level surfaces of F_1 associated with

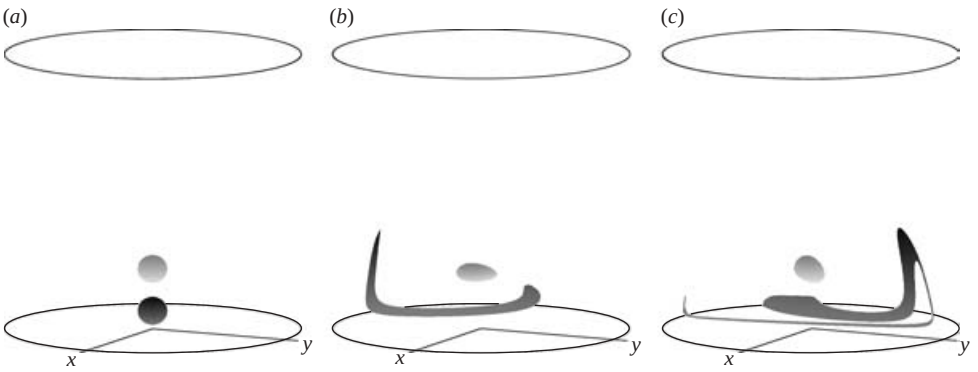

FIGURE 9. Advection of material volumes for forcing protocol A ($D_2 = 5$). (a) $t = 0$, (b) $t = T$, (c) $t = 2T$.

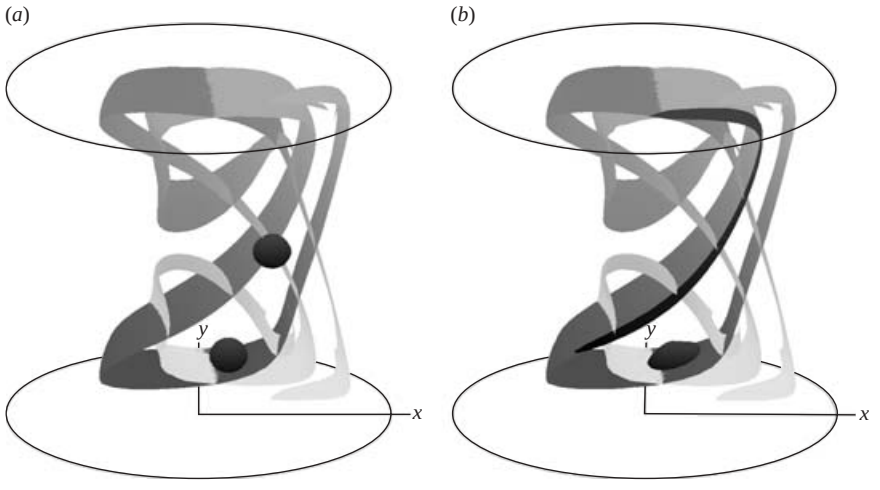

FIGURE 10. Advection of material volumes for forcing protocol B ($D_2 = 5$). (a) $t = 0$, (b) $t = T$.

the poles of the initially spherical blob (projected in the (r, z)-plane coinciding with annulus and disk in figure 8). This geometrical confinement is particularly apparent in figure 9(c).

For protocol B blobs have been released at p_2 (hyperbolic) and p_3 (elliptic) in figure 5(a). The evolution is shown in figure 10 and reveals characteristics similar to those found for protocol A: collapsing of the blob on p_2 onto W^u_{2D} and entrapment of the blob on p_3 in the elliptic tube. Its uniform-type periodic lines and negligible lateral motion allow protocol B to demonstrate this manifold-tube interplay, typical of systems with periodic lines, in an insightful manner. Note that the high stretching rate of protocol B causes the blob on p_2 to almost merge with W^u_{2D} within just one period.

Because of its symmetry S_y, implying planar motion in $y = 0$, protocol B lends itself perfectly to illustrating the link between manifolds and tracer transport. Figure 11 shows the evolution of a circular interface ($r/R = 0.1$) released at an arbitrary location in $y = 0$ in the region occupied by the manifolds, revealing that the interface progressively aligns with the unstable manifold as time proceeds. This alignment is found for any such interface placed in this region and thus exposes the manifold as a 'deformation template' into which arbitrarily placed material objects are asymptotically

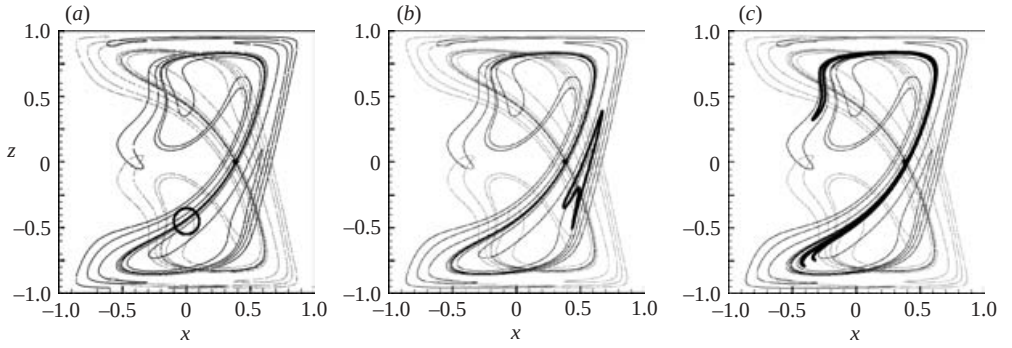

FIGURE 11. Advection of material disk (heavy curve) in plane of symmetry $y = 0$ for forcing protocol B ($D_2 = 5$). The solid and dotted curve represents the unstable and stable manifold, respectively, associated with the periodic point on the hyperbolic line sitting in $y = 0$ (*dot*). (*a*) $t = 0$, (*b*) $t = 3T$, (*c*) $t = 4T$.

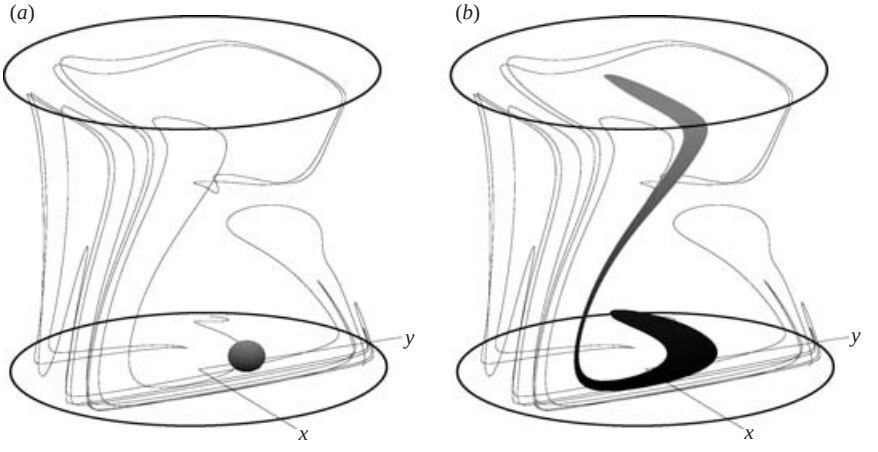

FIGURE 12. Advection of material volumes for forcing protocol C ($D_2 = 5$). (*a*) $t = 0$, (*b*) $t = T$.

shaped as time progresses. This arbitrariness conversely suggests that the advection characteristics connected with a given hyperbolic point/line can be inferred from those of one given object. Similar considerations hold for the transport properties in elliptic tubes and thus suggest that monitoring strategically placed objects, i.e. one object at an arbitrary location (most naturally – but not necessarily – the periodic line/point in question) in each elliptic and hyperbolic region, is sufficient to determine the global transport properties of a given flow, thereby justifying the approach adopted here.

Figure 12 shows a blob placed on the lower periodic point of protocol C at $t = 0$ and $t = T$. For $t \leqslant T$ the blob only partially aligns with W^u_{2D} (curve), which is indicative of an early stage of the advection process (compare with figure 11). At future times, behaviour essentially similar to that illustrated by figure 11 will occur: the blob will be progressively forced into the shape dictated by W^u_{2D} as time advances. The globally chaotic and essentially three-dimensional tracer dynamics of protocol C, as established before, then imply that the blob exhibits truly three-dimensional chaotic advection, which is mirrored in the essentially three-dimensional state of the blob at $t = T$. Note the stark contrast with the essentially two-dimensional situations for protocols A (figure 9) and B (figure 10).

7. Laboratory experiments

Key aspects of the numerical analysis have been validated experimentally via flow visualization (dye advection) and flow measurement (three-dimensional PTV). Three-dimensional PTV measurements of the velocity field and tracer paths of the steady-forcing case – the fundamental building block of the forcing protocols considered – are quantitatively compared with numerical predictions. The blob advection in the time-periodic flows has been tested qualitatively against dye-advection experiments.

7.1. *Steady flow: three-dimensional PTV measurements*

7.1.1. *Data-acquisition procedure*

The fluid was seeded with particles with diameter $d_p = 250\,\mu\text{m}$. In terms of camera resolution (1018×1019 pixels) this translates via $R = 35\,\text{mm} = 350$ pixels into $d_p = 2.5$ pixels, enabling sufficiently accurate particle identification. The cameras operated at a sampling frequency $f = 30\,\text{Hz}$ ($\Delta t_{ptv} = 0.033\,\text{s}$), meaning for the applied wall velocity $U = 4.38\,\text{mm}\,\text{s}^{-1}$ that a wall displacement (and thus maximum particle displacement) $D_{ptv} = 0.145\,\text{mm} \approx 1.5$ pixel occurred between two consecutive PTV images. Since this is insufficient for reliable particle tracking – typical particle excursions in the interior of the cylinder then would take place at (sub)pixel scale – only every fifth image ($D_{ptv} = 0.725\,\text{mm} \approx 7$ pixels and $\Delta t_{ptv} = 0.167\,\text{s}$) has been processed by the tracking algorithm, resulting in significant improvement in performance. In total $P = 230$ successive frames have been obtained, each yielding around 500 velocity vectors. The time-independence of the flow permitted the combination of the vector fields corresponding to each time level into one overall vector field and thus resulted in a total of 127×10^3 velocity vectors. The total time span was $t_P = (P-1)\Delta t_{ptv} = 38.17\,\text{s}$, with $R = 35\,\text{mm}$ resulting in a dimensionless wall displacement $D_2 = Ut_P/R = 4.8$. (Note $D_2 = 4.8$ forms the final leg of the total displacement $D_2 = 1.2 + 4.8 = 6$. The initial leg $D_2 = 1.2$ includes the essentially unsteady start-up stage of the flow that has been excluded from the tracking algorithm.) Vectors $\boldsymbol{u}(\boldsymbol{x})$ satisfying $|\boldsymbol{u}| > U$ and/or $\sqrt{x^2 + y^2} > R$ have been removed (roughly 10% of the total population), leaving a velocity field $\boldsymbol{u}_{ptv}$ comprising $N_{ptv} \approx 114 \times 10^3$ vectors. One-to-one correspondence with the non-dimensional problem has been achieved by transformation of the PTV coordinates to the unit cylinder and rescaling of $\boldsymbol{u}_{ptv}$ such that $U = 1$. Furthermore, data enhancement has been carried through by the addition of boundary vectors, identically meeting the no-slip condition, on an $N_\Gamma \times N_\Gamma$ equidistant grid ($N_\Gamma = \sqrt[3]{N}$) on both endwalls and the mantle. The optimal window size for the interpolation scheme (see § 4.2) was then $\sigma/R = 0.024$.

7.1.2. *Velocity field*

Figure 13 displays the measured velocity field $\overline{\boldsymbol{u}}_{ptv}$ (panel *a*) in comparison to the semi-analytical velocity field $\boldsymbol{u}_a$ following Shankar (1997) (panel *b*) in the plane of symmetry $y = 0$. Note that $\bar{\boldsymbol{u}}_{ptv}$ is attained from $\boldsymbol{u}_{ptv}$ via the Gaussian interpolation scheme (see § 4.2). Overall, both fields exhibit a good qualitative correspondence; significant departures arise only in the lower corner regions. These are inherent in the jump in the boundary velocity at the lower rim of the cylinder. Mathematically, this represents a discontinuity in boundary conditions, which is treated numerically by definition of a narrow transitional region within which the bottom wall velocity $U = 1$ smoothly drops off to $U = 0$ on the bottom rim (see Shankar 1997). Experimentally, a minute gap between the still mantle and the translating bottom wall is allowed, establishing a thin in/outflow layer within which the velocity adjusts from $U = 1$ to $U = 0$ on the respective boundary segments. Both approaches lead to essentially

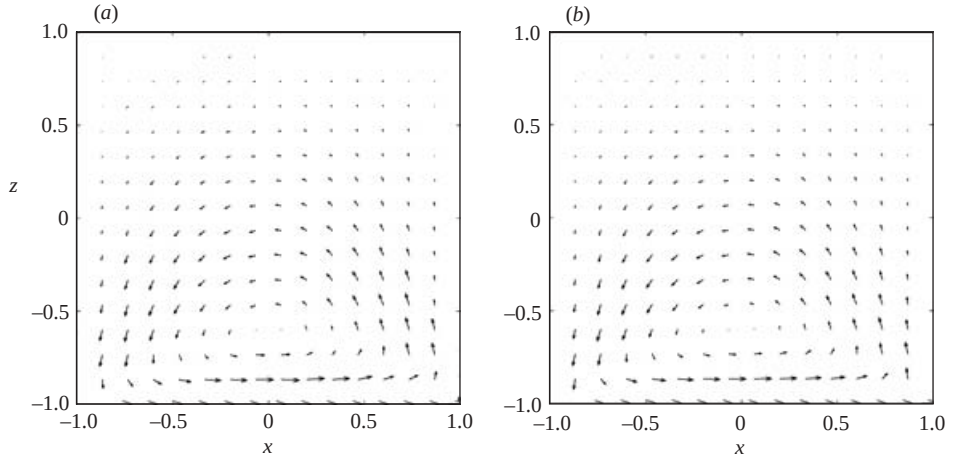

FIGURE 13. Velocity fields in the plane of symmetry $y = 0$. (*a*) Measured velocity field $\bar{\boldsymbol{u}}_{ptv}$. (*b*) Analytical velocity field $\boldsymbol{u}_a$.

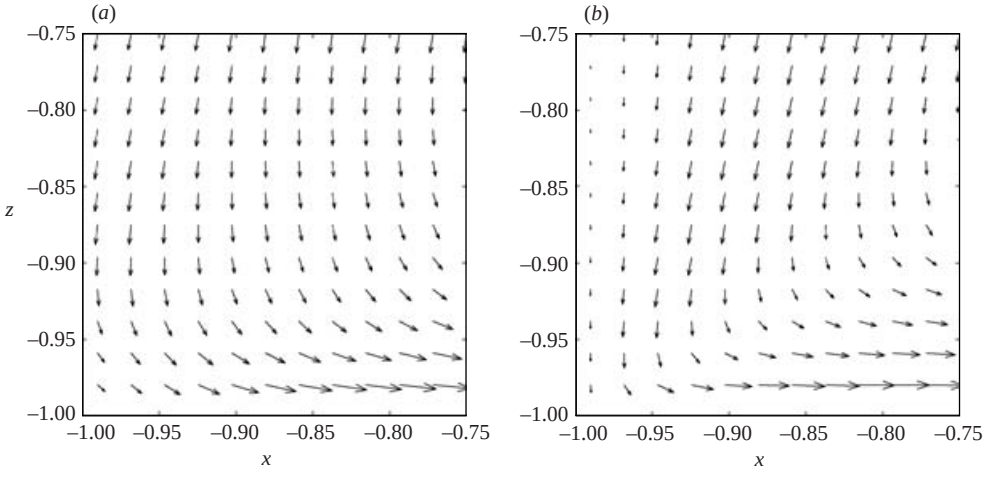

FIGURE 14. Velocity field near the lower left corner in $y = 0$. (*a*) Measured velocity field $\bar{\boldsymbol{u}}_{ptv}$. (*b*) Analytical velocity field $\boldsymbol{u}_a$.

different flow patterns in the bottom-rim region. A close-up of the bottom-rim region is given in figure 14, showing the measured (panel *a*) and semi-analytical (panel *b*) velocity field at the lower-left corner in the plane $y = 0$. Contrary to the internal flow depicted in figure 13, significant differences between measured and semi-analytical fields occur upon approaching the corner. Relative to the semi-analytical field, $\overline{\boldsymbol{u}}_{ptv}$ exhibits a deflection in the positive x-direction due to the inflow of ambient fluid at the lower-left corner through the aforementioned gap.

In addition to the above, a quantitative comparison between the semi-analytical and measured velocity fields has been performed, which is discussed in the following. Introduce the discrepancy vector $\boldsymbol{e}_{tot} = \boldsymbol{u}_{ptv} - \boldsymbol{u}_a$, defining the deviation between the measured ($\boldsymbol{u}_{ptv}$) and predicted ($\boldsymbol{u}_a$) flow field relative to the unit cylinder. The difference between the two velocity fields has two contributions, namely $\boldsymbol{e}_{tot} = \boldsymbol{e}_{ptv} + \boldsymbol{e}_{model}$, accounting for the error induced during data acquisition and data processing ($\boldsymbol{e}_{ptv}$)

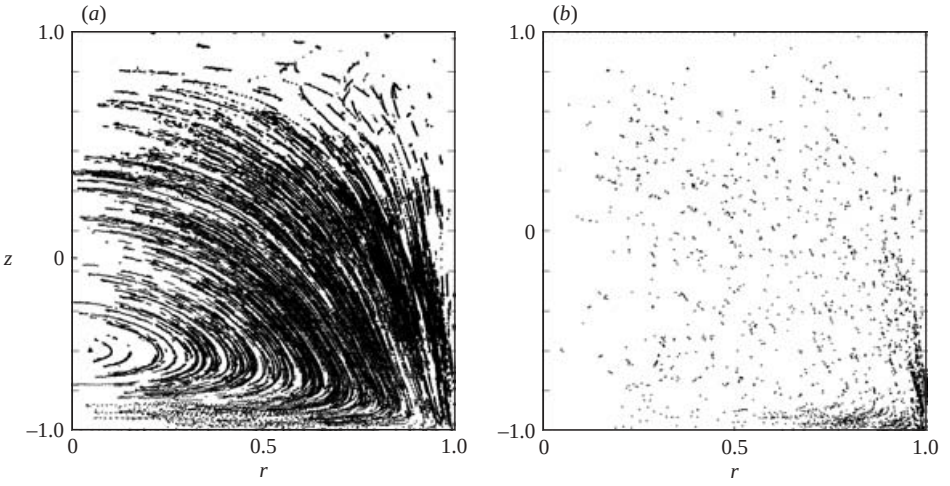

FIGURE 15. Modelling error ϵ_{model} evaluated on the unstructured grid $\boldsymbol{x}_{ptv}$ (projection in the (r, z)-plane). (*a*) $\epsilon_{model} < 5\%$, (*b*) $\epsilon_{model} \geqslant 5\%$.

and the modelling error ($\boldsymbol{e}_{model}$). The former includes measuring errors and algorithmic shortcomings of the three-dimensional PTV procedure. The latter comprises a threefold contribution: approximation errors inherent in (i) the Stokes model and (ii) the solution procedure of Shankar (1997); (iii) interpolation errors induced by the interpolation scheme.

An estimate for $\boldsymbol{e}_{ptv}$ is found in the velocity field $\boldsymbol{E}_{ptv}$ attained for a non-moving bottom wall ($U = 0$); non-zero $\boldsymbol{E}_{ptv}$ then embodies the cumulative noise underlying $\boldsymbol{e}_{ptv}$. Measurements yielded $\boldsymbol{E}_{ptv}$ at roughly 1500 randomly distributed positions and statistical analysis revealed that $e_{ptv} = |\boldsymbol{e}_{ptv}|$, with $\boldsymbol{e}_{ptv} = \boldsymbol{E}_{ptv}/U$ and U of the *moving* wall experiment, formed a normal distribution with average $\mu = 0.0072$ and standard deviation $\sigma = 0.0081$. This suggests the upper bound of the 96%-confidence interval $e_{ptv}^{96} = \mu + 2\sigma = 0.0234$ as an appropriate estimate for the typical experimental error at any given position $\boldsymbol{x}$ (see Chatfield 1978) and suggests the existence of two regimes: regime 1: $e_{tot} \leqslant e_{ptv}^{96} \rightarrow e_{model} = 0$, regime 2: $e_{tot} > e_{ptv}^{96} \rightarrow e_{model} = e_{tot} - e_{ptv}^{96}$. In regime 1, the experimental error $\boldsymbol{e}_{ptv}$ fully accounts for the discrepancy between measured and predicted velocity field and, ergo, the modelling error is insignificant in this region ($\boldsymbol{e}_{model} = 0$). For regime 2, extraneous effects alone are insufficient to explain the attained deviation and thus $\boldsymbol{e}_{model} > 0$.

Error analysis has been carried out on the three-dimensional unstructured grid $\boldsymbol{x}_{ptv}$ – thus ruling out possible interpolation errors – in terms of the relative modelling error $\epsilon_{model} = e_{model}/|\boldsymbol{u}_a| \times 100\%$ and the outcome has been divided into two categories: (i) $\epsilon_{model} < 5\%$ (including $\epsilon_{model} = 0$ for regime 1) and (ii) $\epsilon_{model} \geqslant 5\%$. The error distribution, projected into the (r, z)-plane, is shown in figure 15 and reveals that significant modelling errors (regime 2) concentrate in the bottom-rim region. Note that figures 15(*a*) and 15(*b*) contain 94% and 6%, respectively, of the total number of nodes. These findings align with the previously advanced conclusions that the discrepancy between numerical and experimental velocity fields ensues primarily from the essentially different bottom-rim situations. In the non-inertial limit, disturbances (here discrepancies in the lower-corner flow field) manifest themselves most prominently in the compact region surrounding their origin (here the bottom-rim area); further away dissipative effects result in their rapid decay. This explains the

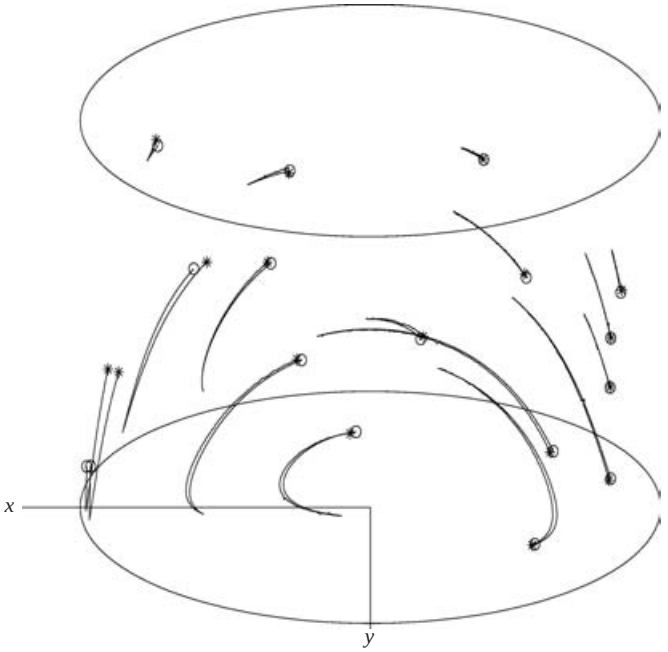

FIGURE 16. Comparison of measured ($\boldsymbol{X}^{ptv}$) and numerical ($\boldsymbol{X}^{e}$) trajectories. The symbols indicate the final positions (∗, $\boldsymbol{X}^{ptv}$; ○, $\boldsymbol{X}^{a}$).

peaking in the bottom-rim region and rapid diminishing outside it of ϵ_{model}. A similar analysis on a structured grid in the plane $y = 0$ proved consistent with the above (see Speetjens 2001). Note that this implies that interpolation errors inherent in the use of structured grids are insignificant for the total error. Overall, the above analysis revealed a good quantitative agreement between measured and semi-analytical velocity fields. Accounting for measuring errors, the deviation outside the compact bottom-rim region typically remained within the 5%-limit.

7.1.3. *Trajectories*

Experimental particle paths $\boldsymbol{X}_t^{ptv}(\boldsymbol{x}_0)$ have been compared with numerical tracer paths $\boldsymbol{X}_t^{a}(\boldsymbol{x}_0)$ for identical initial position $\boldsymbol{x}_0$ and time span $t_p = (p-1)\Delta t_{ptv}$, with $1 \leqslant p \leqslant P$ and P and Δt_{ptv} as before. Figure 16 shows $\boldsymbol{X}_t^{ptv}$ and $\boldsymbol{X}_t^{a}$ for a number of paths in the time-span range $t_{200} \leqslant t_p \leqslant t_{230}$ and shows that the computed paths almost shadow their real-life counterparts. Significant departures occur only for the three paths originating from the lower-left corner due to the previously addressed bottom-rim situations. For the remaining paths $|\boldsymbol{x}_{ptv}(t) - \boldsymbol{x}_a(t)|/R \leqslant 0.015$, implying an outstanding agreement between computed and measured paths at any given time $t \leqslant t_p$.

In § 5.1 the projection of three-dimensional trajectories $\boldsymbol{X}^a$ onto the (r, z)-plane is shown to coincide with the streamline portrait in the plane $y = 0$ due to the particular structure of the semi-analytical velocity field $\boldsymbol{u}_a$. Based on the good agreement between $\boldsymbol{u}_a$ and $\boldsymbol{u}_{ptv}$ found before, one might expect this projection property to hold for the measured paths as well. Introduce, in order to verify this conjecture, the Fourier

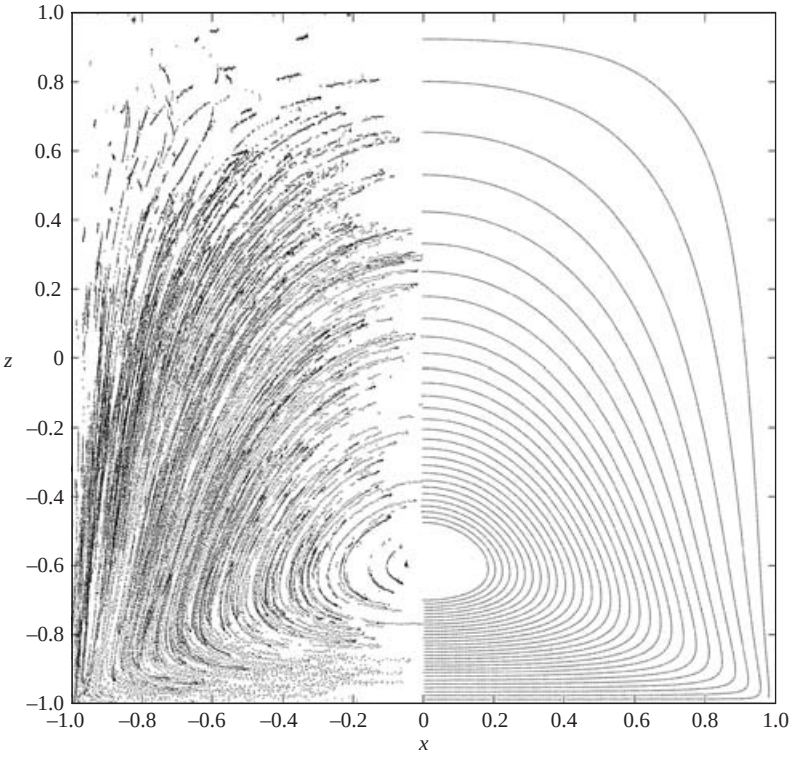

FIGURE 17. Streamline portrait in the plane of symmetry $y=0$ (*a*) $\boldsymbol{X}^{ptv}$, (*b*) $\boldsymbol{X}^{a}$.

expansion

$$\boldsymbol{u}(\boldsymbol{x}) = 2\left[\sum_{m=0}^{\infty} \boldsymbol{u}_{Rm}\cos m\theta + \boldsymbol{u}_{Im}\sin m\theta\right], \tag{7.1}$$

for a real variable $\boldsymbol{u}$, with Fourier spectrum $\widetilde{\boldsymbol{u}}_m = \boldsymbol{u}_{Rm} + \mathrm{i}\boldsymbol{u}_{Im}$ (see Canuto *et al.* 1987). The spectrum for $\boldsymbol{u}_a$ follows from (5.1) and, in a qualitative sense, is

$$\widetilde{u}_{r,z_{Rm}} = \mathsf{u}_{r,z}/2, \quad \widetilde{u}_{r,z_{Im}} = 0, \quad \widetilde{u}_{\theta_{Rm}} = 0, \quad \widetilde{u}_{\theta_{Im}} = \mathsf{u}_{\theta}/2, \tag{7.2}$$

for $m=1$ and $\widetilde{\boldsymbol{u}}_a = \boldsymbol{0}$ for $m \neq 1$. For the spectrum of $\boldsymbol{u}_{ptv}$

$$\frac{|u_{r,z_{I1}}|}{|u_{r,z_{R1}}|} \sim O(10^{-2}), \quad \frac{|u_{\theta_{R1}}|}{|u_{\theta_{I1}}|} \sim O(10^{-2}), \quad \frac{|\widetilde{\boldsymbol{u}}_m|}{|\widetilde{\boldsymbol{u}}_1|} \sim O(10^{-2}) \text{ for } m \neq 1, \tag{7.3}$$

is found, isolating $m=1$ as the dominant Fourier mode. Accounting for the experimental error $e_{ptv} \sim O(10^{-2})$, the spectra (7.2) and (7.3) to a good approximation coincide, meaning that $\boldsymbol{u}_{ptv}$ is in good agreement with the form (5.1), in turn suggesting that the aforementioned projection property is indeed valid for $\boldsymbol{X}^{ptv}$. Figure 17 graphically combines the projected trajectories $\boldsymbol{X}^{ptv}$ (left half) and the streamlines $\boldsymbol{X}^{a}$ in $y=0$ (right half). Both halves connect smoothly and assume a symmetrical arrangement about the axis $x=0$, thus forming a good representation of the streamline portrait at $y=0$. This further substantiates the good agreement between numerical and experimental paths. Near the top the left-right correspondence is lost due to $\boldsymbol{u}_{ptv} \sim O(\boldsymbol{e}_{ptv})$. Figure 18 provides a close-up of the lower-corner region, showing that the good qualitative agreement between measured (panel *a*) and computed (panel *b*) streamline patterns persists at smaller-scale levels. In the bottom-rim region,

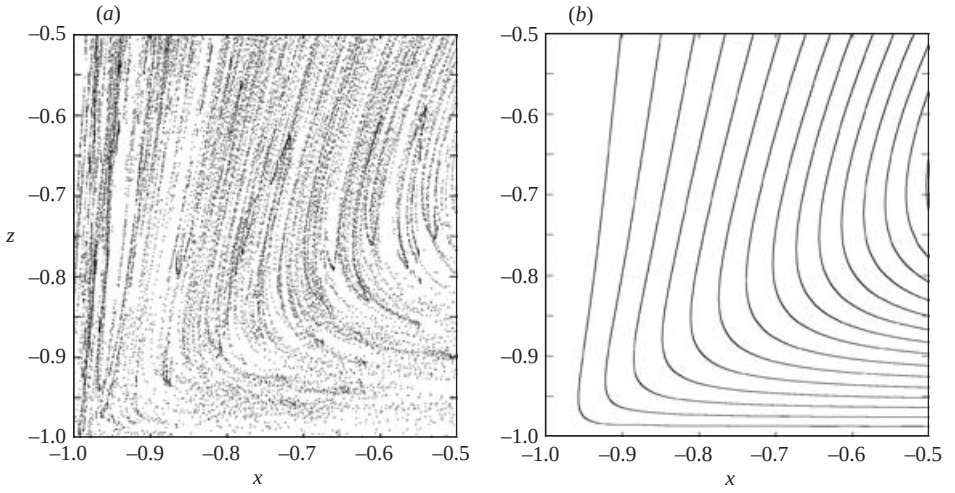

FIGURE 18. Streamline portrait near the left corner in the plane of symmetry $y = 0$. (*a*) $\boldsymbol{X}^{ptv}$, (*b*) $\boldsymbol{X}^{a}$.

$\boldsymbol{X}^{ptv}$ becomes less pronounced and thus difficult to compare with $\boldsymbol{X}^{a}$. In this area significant discrepancies are to be expected on grounds discussed before.

7.2. *Time-periodic flows: dye-advection experiments*

The numerical blob advection discussed in § 6.2 has been mimicked in the laboratory set-up by means of dye experiments. Blobs of passive dye were placed on suspected periodic points/lines and monitored for one period of the forcing protocol ($D_2 = 5$). Photographs of the blobs were taken at several stages in the forcing cycle and qualitatively compared with the numerical predictions.

For protocol *A*, blue and red dye was injected at the position of the lower and upper blob, respectively, in figure 9(*a*). The state of the blobs is shown in figure 19 at $t = 0, T/2, T$ for experiments (top row) and computations (bottom row), viewing the (x, z)-plane in the negative y-direction. At all times an outstanding agreement between predictions and observations is attained; the blobs respond exactly as predicted. The red blob (elliptic segment of the periodic line) remains almost perfectly intact, apart from the minor horizontal elongation at $t = T/2$. The blue blob (hyperbolic segment) is gradually wrapped around its red companion while converging on the unstable manifold. Note that the blue blob thus visualizes that manifold.

For forcing protocol *B*, dye experiments, in an equivalent manner, sought to validate the situation in figure 10. Red and blue dye was placed on the lower elliptic line and the hyperbolic line, respectively, and its advection is monitored for one period. The results are given in figure 20, with lay-out and viewpoint as before. Similar to protocol *A*, good qualitative agreement between numerical and experimental results is attained. Significant deviation is found only for the red blob, the observed deformation of which is notably higher than predicted numerically, and is believed to result from both proximity and high deformation rate – at the blob location the stretching rate of the unstable manifold is $\lambda \simeq 14$, compared to $\lambda \simeq 2$ for protocol *A* – of the adjoining hyperbolic region (see Speetjens 2001). This suggests an extreme sensitivity of the blob evolution to mismatches in initial conditions. The rightward-pointing tail of the red blob in figure 20(*a*), signifying departure from sphericity, for instance partially intrudes into the hyperbolic region and is therefore exposed to substantial stretching

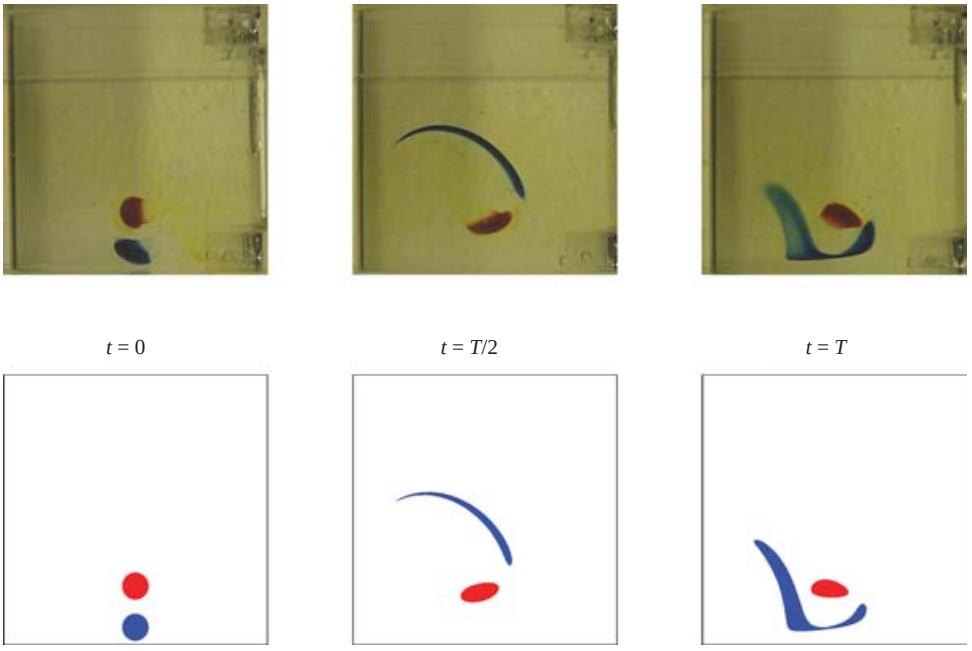

FIGURE 19. Experimental vs. numerical results for forcing protocol A (viewing in the negative y-direction).

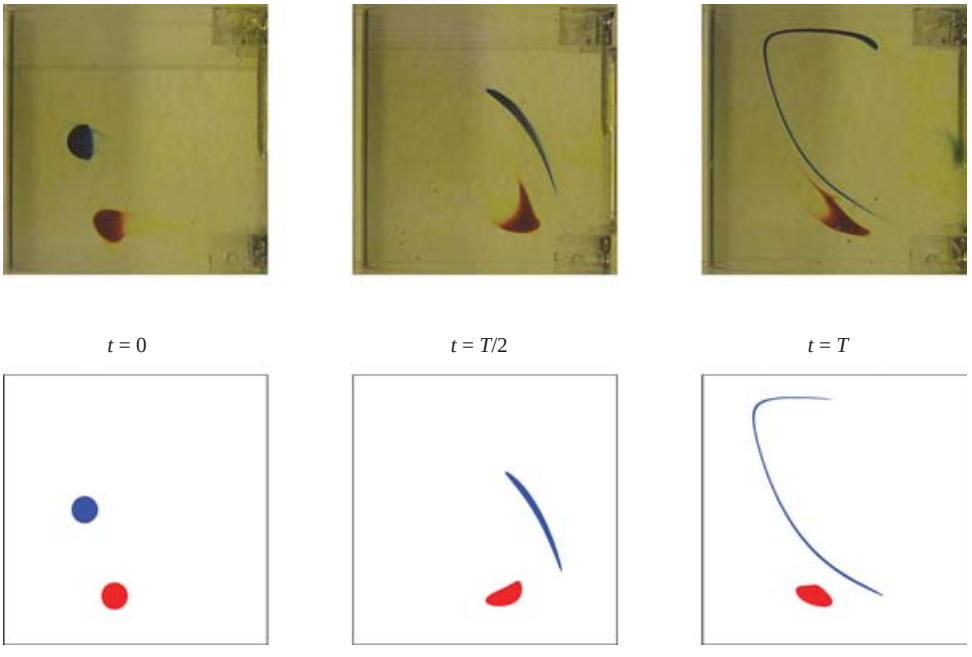

FIGURE 20. Experimental vs. numerical results for forcing protocol B (viewing in the negative y-direction).

rates (as is apparent from figure 20). This largely accounts for the discrepancy between experimental observations and numerical predictions on the red blob. Note that, as for protocol A, the blue blob outlines part of the unstable manifold of the hyperbolic line.

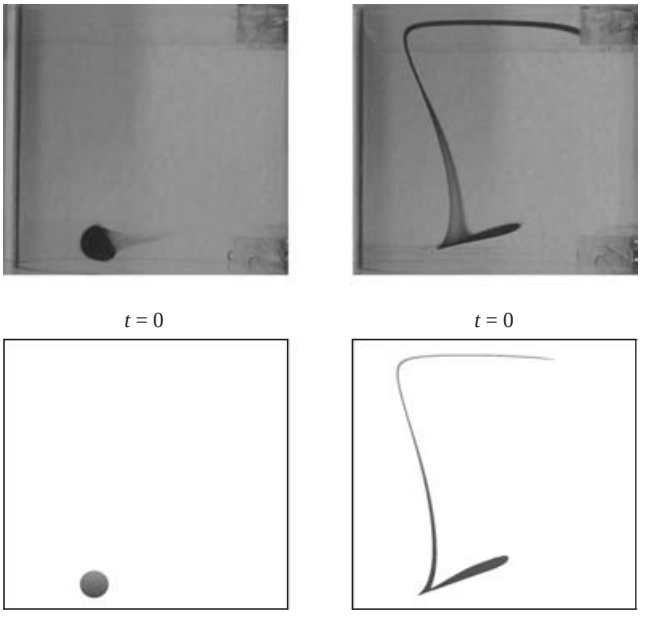

FIGURE 21. Experimental vs. numerical results for forcing protocol *C* (viewing in the negative *y*-direction).

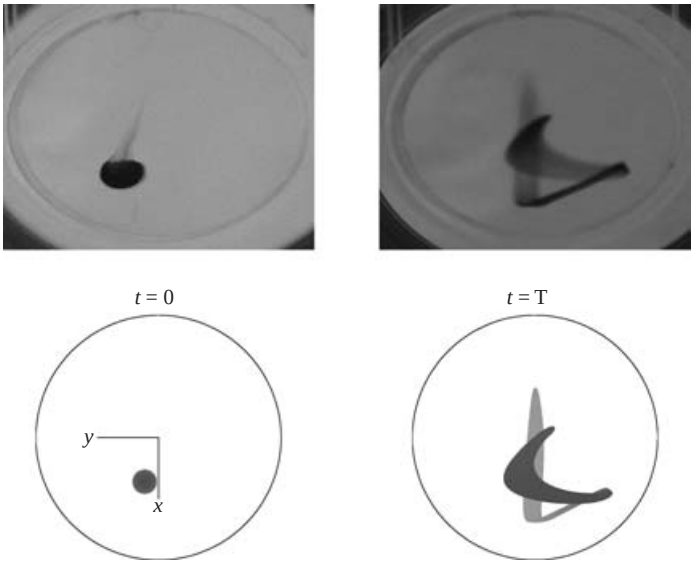

FIGURE 22. Experimental vs. numerical results for forcing protocol *C* (viewing in the positive *z*-direction).

Forcing protocol *C* hosts isolated periodic points and thus has a flow topology of far greater complexity than those found for the above periodic-line systems. Experimental validation of the blob advection in this configuration thus is considerably more challenging than in the previous cases. The experiments focused on the situation in figure 12 and resulted in the images shown in figure 21 (layout as before) and figure 22 (viewing in the positive *z*-direction). Comparison of the experimental and numerical

evolutions reveals even for the intricate and essentially three-dimensional structure of the blob at $t = T$ an outstanding agreement.

The dye-advection experiments displayed a high degree of reproducibility and robustness. Repeated experiments yielded practically identical outcomes for each protocol; minor differences between numerics and experiments are believed to result predominantly from minute mismatches in initial conditions.

8. Conclusions

The work presented in this paper concerns a numerical and experimental investigation of the advection of passive tracers in a non-inertial cylinder flow. One steady and three time-periodic flows have been considered, the former constituting the elementary building block of the latter, serving as prototypical three-dimensional viscous mixing flows. The advection problem is tackled from a topological standpoint by concentrating on the role of coherent structures in the web of tracer paths ('flow topology') in the process of tracer transport.

The numerical study involved determination of flow topology and corresponding transport properties. Symmetries emerged as pivotal in this analysis by constituting an invaluable vehicle for robust and efficient identification of coherent structures, thus demonstrating the potential of symmetry-based approaches in the present context. Three out of four flow topologies followed readily from universal symmetry concepts; in the fourth case symmetries translated into a compact case-specific identification procedure. An important corollary of time-reversal symmetries is found in that in bounded systems they invariably imply periodic lines.

The tracer dynamics encompassed three fundamental states: non-chaotic (steady flow); (quasi-)two-dimensional locally chaotic (protocols A and B); three-dimensional globally chaotic (protocol C). The nature of the tracer transport proved inextricably linked to the topological properties of periodic structures and associated coherent structures (manifolds and tubes). The steady case included a family of elliptic tubes centred on an elliptic (stagnation) line, within which shear-like fluid flow and, inherently, non-chaotic tracer dynamics occurred. Protocols A and B hosted elliptic-type and hyperbolic-type periodic lines and, in consequence, accommodated coexisting chaotic and non-chaotic regions with (quasi-)two-dimensional dynamics. The former identified with the region occupied by transversally interacting manifolds of hyperbolic (segments of) periodic lines; the latter coincided with elliptic tubes, centred on elliptic (segments of) periodic lines, entrenched in chaotic regions of the previous kind. The elliptic tubes comprised families of concentric impenetrable surfaces, akin to the steady case, acting as transport barriers and thus obstructing global tracer dispersion. Protocol C hosted isolated periodic points, resulting in a flow topology devoid of transport barriers that consequently permitted unrestricted three-dimensional chaotic advection.

Time variation in the external forcing formed an essential ingredient for attaining chaotic tracer motion in the present configuration. It established the repeated reorientation of the flow required for obtaining non-closed tracer paths, thus paving the way to chaotic advection. (For steady forcing paths are closed and thus non-chaotic.) Time-periodic forcing is particularly suitable in this respect in that it offers a way for systematic reorientation for arbitrary time spans.

Examination of finite-size material objects exposed, similar to the findings on individual tracers, transport properties and deformation patterns governed entirely by the flow topology. Objects entrapped in elliptic tubes exhibited shear-like deformation

in the annular region between tubes, essentially equivalent to that found for the steady case. Objects released in the zone of influence of manifolds progressively aligned with the unstable manifold, thus designating the latter as a 'deformation template' into which objects are asymptotically shaped.

Laboratory experiments validated several key aspects of the numerical analysis. Flow measurements on the steady flow revealed good (quantitative and qualitative) agreement between the measured and semi-analytical velocity field. Moreover, an outstanding correspondence between measured and computed trajectories has been found. Flow visualization showed good qualitative correspondence between observed and simulated advection of finite-size material objects. Overall, predictions and experiments agreed such that the computational results qualify as representative of real-life phenomena.

The conclusions drawn above have several potential spin-offs to industrial viscous mixing flows, a key motivator for the present work, for which effective mixing is the principal goal. The study advanced periodic lines as indicative of two-dimensional dynamics and thus, in the scope of time-periodic systems, as synonymous with inefficient mixing. Global three-dimensional dispersion, the targeted state, is achieved only in systems which exclusively host isolated periodic points. Design codes for mixing machinery involving time-periodic forcing (e.g. by alternately activated impellers) must thus aim to avoid periodic lines. It is here that the connection between periodic lines and time-reversal reflectional symmetries comes into play. The latter imply the former; the symmetries signify periodic lines and inefficient mixing. Isolation of symmetries requires only gross knowledge of flow and geometry and thus is feasible during early design stages. Symmetry analysis therefore is a powerful design tool that should form an integral part in the development of mixing devices.

M. F. M. S. gratefully acknowledges financial support from the Dutch Foundation of Fundamental Research on Matter (FOM). The authors wish to express their gratitude to Volodya Malyuga and Slava Meleshko for the numerous fruitful scientific discussions, to Gert van der Plas for the technical support concerning the flow measurements, and to the Section of Energy Technology (Department of Mechanical Engineering, Eindhoven University of Technology) for making available their PTV data-acquisition system.

REFERENCES

Abraham, R. H. & Shaw, C. D. 1982 *Dynamics: The Geometry of Behavior*. Aerial Press, Santa Cruz.

Agüi, J. C. & Jiménez, J. 1987 On the performance of particle tracking. *J. Fluid Mech.* **185**, 447–468.

Anderson, P. D., Galaktionov, O. S., Peters, G. W. M., van de Vosse F. N. & Meijer, H. E. H. 1999 Analysis of mixing in three-dimensional time-periodic cavity flows. *J. Fluid Mech.* **386**, 149–166.

Aref, H. 1984 Stirring by chaotic advection. *J. Fluid Mech.* **143**, 1–21.

Aref, H. 1994 Chaotic advection in perspective. *Chaos, Solitons & Fractals* **4**, 745–748.

Aref, H. & Balachandar, S. 1986 Chaotic advection in a Stokes flow. *Phys. Fluids* **29**, 3515–3521.

Arnol'd, V. I. 1965 Sur la topologie des écoulements stationnaires des fluides parfait. *C. R. Acad. Sci. Paris* A **261**, 17–20.

Arnol'd, V. I. 1978 *Mathematical Methods of Classical Mechanics*. Springer.

Bajer, K. 1994 Hamiltonian formulation of the equations of streamlines in three-dimensional steady flows. *Chaos, Solitons & Fractals* **4**, 895–911.

Bajer, K. & Moffatt, H. K. 1990 On a class of steady confined Stokes flows with chaotic streamlines. *J. Fluid Mech.* **212**, 337–363.

Beigie, D., Leonard, A. & Wiggins, S. 1994 Invariant manifold template for chaotic advection. *Chaos, Solitons & Fractals* **4**, 749–868.

Brouwer, L. E. J. 1911 Über Abbildung von Mannigfaltigkeiten. *Math. Annalen* **71**, 97–115. Also in *Collected works/L. E. J. Brouwer*, vol. 2 (ed. M. Freudenthal), pp. 454–472, North-Holland.

Canuto, C., Hussaini, M. Y., Quarteroni, A. & Zang, T. A. 1987 *Spectral Methods in Fluid Dynamics*. Springer.

Cartwright, J. H. E., Feingold, M. & Piro, O. 1996 Chaotic advection in three-dimensional unsteady incompressible laminar flow. *J. Fluid Mech.* **316**, 259–284.

Chatfield, C. 1978 *Statistics for Technology: A Course in Applied Statistics*. Chapman & Hall.

Cheng, C. Q. & Sun, Y. S. 1990 Existence of invariant tori in three-dimensional measure preserving mappings. *Celest. Mech.* **47**, 275–292.

Chien, W. L., Rising, H. & Ottino, J. M. 1986 Laminar mixing and chaotic mixing in several cavity flows. *J. Fluid Mech.* **170**, 355–377.

Chong, M. S., Perry, A. E. & Cantwell, B. J. 1990 A general classification of three-dimensional flow fields. *Phys. Fluids* A **2**, 765–777.

Croom, F. H. 1978 *Basic Concepts of Algebraic Topology*. Springer.

Dombre, T., Frisch, U., Greene, J. M., Hénon, M., Mehr, A. & Soward, A. M. 1986 Chaotic streamlines in the ABC flows. *J. Fluid Mech.* **167**, 353–391.

Feingold, M., Kadanoff, L. P. & Piro, O. 1987 A way to connect fluid dynamics to dynamical systems: passive scalars. In *Fractal Aspects of Materials: Disordered Systems* (ed. A. J. Hurd, D. A. Weitz & B. B. Mandelbrot), pp. 203–205. Materials Research Society.

Feingold, M., Kadanoff, L. P. & Piro, O. 1988 Passive scalars, three-dimensional volume-preserving maps and chaos. *J. Staist. Phys.* **50**, 529–565.

Fountain, G. O., Khakhar, D. V., Mezić, I. & Ottino, J. M. 2000 Chaotic mixing in a bounded three-dimensional flow. *J. Fluid Mech.* **417**, 265–301.

Fountain, G. O., Khakhar, D. V. & Ottino J. M. 1998 Visualization of three-dimensional chaos. *Science* **281**, 683–685.

Franjione, J. G., Leong, C. W. & Ottino, J. M. 1989 Symmetries within chaos: a route to effective mixing. *Phys. Fluids* A **1**, 1772–1783.

Guckenheimer, J. & Holmes, P. 1983 *Nonlinear Oscillations, Dynamical Systems and Bifurcations of Vector Fields*. Springer.

Hackborn, W. W., Ulucakli, M. E. & Yuster, T. 1997 A theoretical and experimental study of hyperbolic and degenerate mixing regions in a chaotic Stokes flow. *J. Fluid Mech.* **346**, 23–48.

Harnby, N., Edwards, M. F. & Nienow, A. W. 1992 *Mixing in the Process Industries*, 2nd Edn. Butterworth-Heinemann.

Kieft, R. N., Schreel, K. R. A. M., van der Plas, G. A. J. & Rindt, C. C. M. 2002 The application of a 3D-PTV algorithm to a mixed convection flow. *Exps. Fluids* **33**, 603–611.

King, G. 1998 Towards a science of mixing. *Physics World*, 23–24.

Krasnopolskaya, T. S., Meleshko, V. V., Peters, G. W. M. & Meijer, H. E. H. 1999 Mixing in Stokes flow in an annular wedge cavity. *Eur. J. Mech./*B *Fluids* **18**, 793–822.

Kruijt, P. G. M., Galaktionov, O. S., Anderson, P. D., Peters, G. W. M. & Meijer, H. E. H. 2001 Analyzing mixing in periodic flows by distribution matrices: mapping method. *AIChE J.* **47**, 1005–1015.

Kusch, H. A. & Ottino, J. M. 1992 Experiments on mixing in continuous chaotic flows. *J. Fluid Mech.* **236**, 319–348.

MacKay, R. S. 1994 Transport in 3D volume-preserving flows. *J. Nonlinear Sci.* **4**, 329–354.

Malyuga, V. S., Meleshko, V. V., Speetjens, M. F. M., Clercx, H. J. H. & van Heijst, G. J. F. 2002 Mixing in the Stokes flow in a cylindrical container. *Proc. R. Soc. Lond.* A **458**, 1867–1885.

Meleshko, V. V. 1994 Nonstirring motion of an inviscid fluid by a point vortex in a rectangle *Phys. Fluids* **6**, 6–8.

Meleshko, V. V. & Aref, H. 1996 A blinking rotlet model for chaotic advection *Phys. Fluids* **8**, 3215–3217.

Meleshko, V. V., Galaktionov, O. S., Peters, G. W. M. & Meijer, H. E. H. 1999 Three-dimensional mixing in Stokes flow: the partitioned pipe mixer problem revisited. *Eur. J. Mech./*B *Fluids* **18**, 783–792.

Meleshko, V. V., Malyuga, V. S. & Gomilko, A. M. 2000 Steady Stokes flow in a finite cylinder. *Proc. R. Soc. Lond.* A **456**, 1741–1758.

Meleshko, V. V. & Peters, G. W. M. 1996 Periodic points for two-dimensional Stokes flow in a rectangular cavity. *Phys. Lett.* A **216**, 87–96.

Mezić, I. & Wiggins, S. 1994 On the integrability and perturbation of three-dimensional fluid flows with symmetry. *J. Nonlinear Sci.* **4**, 157–194.

Miles, K. C., Nagarajan, B. & Zumbrunnen, D. A. 1995 Three-dimensional chaotic mixing of fluids in a cylindrical cavity. *Trans. ASME: J. Fluids Engng* **117**, 582–588.

Muzzio, F. J., Swanson, P. D. & Ottino, J. M. 1991 The statistics of stretching and stirring in chaotic flows. *Phys. Fluids* A **3**, 822–834.

Ott, E. 2002 *Chaos in Dynamical Systems*, 2nd Edn. Cambridge University Press.

Ottino, J. M. 1989 *The Kinematics of Mixing: Stretching, Chaos and Transport*. Cambridge University Press.

Ottino, J. M. 1990 Mixing, chaotic advection and turbulence. *Annu. Rev. Fluid Mech.* **22**, 207–253.

Ottino, J. M., Jana, S. C. & Chakravarthy, V. S. 1994 From Reynolds's stretching and folding to mixing studies using horseshoe maps. *Phys. Fluids* **6**, 685–699.

Ottino, J. M., Leong, C. W., Rising, H. & Swanson, P. D. 1988 Morphological structures produced by mixing in chaotic flows. *Nature* **333**, 419–425.

Ottino, J. M., Muzzio, F. J., Tjahjadi, M., Franjione, J. G., Jana, S. C. & Kusch, H. A. 1992 Chaos, symmetry and self-similarity: exploiting order and disorder in mixing processes. *Science* **257**, 754–760.

Poincaré, H. 1892 *Méthodes Nouvelles de la Mécanique Céleste*. Gauthier-Villars. Translated as *New Methods of Celestial Mechanics* (ed. D. L. Goroff), American Institute of Physics.

Schreel, K. R. A. M., van der Plas, G. A. J. & Kieft, R. 2000 Accuracy of a 3D particle tracking velocimetry method. In *Proc. 9th Intl Symp. on Flow Visualization* (ed. I. Grant), paper 310, published on CD (ISBN 095339117).

Shankar, P. N. 1997 Three-dimensional eddy structure in a cylindrical container. *J. Fluid Mech.* **342**, 97–118.

Shankar, P. N. & Deshpande, M. D. 2000 Fluid mechanics in the driven cavity. *Annu. Rev. Fluid Mech.* **32**, 93–136.

Speetjens, M. F. M. 2001 Three-dimensional chaotic advection in a cylindrical domain. PhD thesis, Eindhoven University of Technology.

Strang, G. 1976 *Linear Algebra and its Applications*. Harcourt Brace Jovanovich, San Diego.